



**HAL**  
open science

## Surface and sub-surface flow estimation at high temporal resolution using deep neural networks

Ather Abbas, Sangsoo Baek, Minjeong Kim, Mayzonee Ligaray, Olivier Ribolzi, Norbert Silvera, Joong-Hyuk Min, Laurie Boithias, Kyung Hwa Cho

► **To cite this version:**

Ather Abbas, Sangsoo Baek, Minjeong Kim, Mayzonee Ligaray, Olivier Ribolzi, et al.. Surface and sub-surface flow estimation at high temporal resolution using deep neural networks. *Journal of Hydrology*, 2020, 590, pp.125370 -. 10.1016/j.jhydrol.2020.125370 . hal-03491424

**HAL Id: hal-03491424**

**<https://hal.science/hal-03491424>**

Submitted on 22 Aug 2022

**HAL** is a multi-disciplinary open access archive for the deposit and dissemination of scientific research documents, whether they are published or not. The documents may come from teaching and research institutions in France or abroad, or from public or private research centers.

L'archive ouverte pluridisciplinaire **HAL**, est destinée au dépôt et à la diffusion de documents scientifiques de niveau recherche, publiés ou non, émanant des établissements d'enseignement et de recherche français ou étrangers, des laboratoires publics ou privés.



Distributed under a Creative Commons Attribution - NonCommercial 4.0 International License

1 Surface and sub-surface flow estimation at high temporal  
2 resolution using deep neural networks

3 *Ather Abbas*<sup>1\*</sup>, *Sangsoo Baek*<sup>1\*</sup>, *Minjeong Kim*<sup>1</sup>, *Mayzonee Ligaray*<sup>1</sup>, *Olivier Ribolzi*<sup>2</sup>,  
4 *Norbert Silvera*<sup>3</sup>, *Joong-Hyuk Min*<sup>4</sup>, *Laurie Boithias*<sup>2†</sup>, *Kyung Hwa Cho*<sup>1†</sup>

5 <sup>1</sup> School of Urban and Environmental Engineering, Ulsan National Institute of Science  
6 and Technology, Ulsan, 689-798, Republic of Korea

7 <sup>2</sup> Geosciences Environnement Toulouse, Université de Toulouse, CNRS, IRD, UPS,  
8 31400 Toulouse, France

9 <sup>3</sup> iEES-Paris, UMR 7618 (IRD, CNRS, UPMC), Centre IRD d'Ile de France – 32, avenue  
10 Henri Varagnat, 93143 Bondy cedex, France

11 <sup>4</sup> Water Quality Assessment Research Division, National Institute of Environmental  
12 Research, Environmental Research Complex, Hwangyeong-ro 42, Seo-gu, Incheon 22689, Korea

13

14 *\*Co-first authors: Ather Abbas, Sangsoo Baek*

15 *† Corresponding author: Kyung Hwa Cho (khcho@unist.ac.kr), Laurie Boithias*  
16 *([laurie.boithias@get.omp.eu](mailto:laurie.boithias@get.omp.eu))*

17

18

Manuscript for

19

*Journal of Hydrology*

20 **Abstract**

21           Recent intensification in climate change have resulted in the rise of hydrological extreme  
22 events. This demands modeling of hydrological processes at high temporal resolution to better  
23 understand flow patterns in catchments. To model surface and sub-surface flows in a catchment  
24 we utilized a physically based model called Hydrological Simulated Program-FORTRAN and  
25 two deep learning-based models. One deep learning model consisted of only one long short-term  
26 memory (simple LSTM), whereas the other model simulated processes in each hydrological  
27 response unit (HRU) by defining one separate LSTM for each HRU (HRU-based LSTM). The  
28 models use environmental time-series data and two-dimensional spatial data to predict surface  
29 and sub-surface flows at 6-minute time step simultaneously. We tested our models in a tropical  
30 humid headwater catchment in northern Lao PDR and compared their performances. Our results  
31 showed that the simple LSTM model outperformed the other models on surface runoff prediction  
32 with the lowest MSE ( $7.4e-5 \text{ m}^3\text{s}^{-1}$ ), whereas HRU-based LSTM model better predicted patterns  
33 and slopes in sub-surface flow in comparison with the other models by having the smallest MSE  
34 value ( $3.2e-4 \text{ m}^3\text{s}^{-1}$ ). This study demonstrated the performance of a deep learning model when  
35 simulating hydrological cycle with high temporal resolution.

36

37           KEYWORDS: Deep learning model, Long short-term memory (LSTM), Sub-surface  
38 flow, Surface runoff, Hydrological Simulated Program-FORTRAN

## 39 **1 Introduction**

40 Recently, increase in precipitation extreme events has been witnessed at global scale  
41 (Papalexiou and Montanari, 2019). Roxy et al., (2017) documented threefold increase in rainfall  
42 events from 1950 to 2017 in central India. The International Disaster Database noted global  
43 annual loss of over \$30 billion as a result of floods in last decade (Roxy et al., 2017). To  
44 understand the hydrological complexity of flash floods, we need to model hydrological  
45 phenomena at sub-daily time-step (Jodar-Abellan et al., 2019). Reynolds et al., (2017) has also  
46 stressed the need for streamflow prediction at a sub-daily time-step for flood forecasting in  
47 medium-sized (10-1000 Km<sup>2</sup>) catchments due to small concentration time. The identification of  
48 water components contributing to total streamflow plays a key role in understanding bio-  
49 geochemical cycles and transport processes at catchment scale (Burns and Kendall, 2002).  
50 Accurate estimation of sub-surface water flow is critical in time-continuous models in  
51 comparison with event-based models due to the dominance of groundwater in continuous  
52 rainfall-runoff models (Huang et al., 2016; Guse et al., 2014).

53 Several research groups have developed catchment-scale modeling tools, such as the  
54 Soil & Water Assessment Tool (SWAT) (Arnold and Fohrer, 2005), the Stormwater  
55 Management Model (SWMM) (Rossman, 2010), and the Hydrological Simulation Program-  
56 FORTRAN (HSPF) (Bicknell et al., 2001). However, most of these hydrological models are used  
57 for a single rainfall event or daily simulation because sub-hourly simulation is complex and time  
58 consuming (Bennett et al., 2016). Jeong et al., (2010) improved the SWAT model to simulate  
59 stream discharge at a sub-hourly time-step; however, some processes in their improved model,  
60 such as baseflow and lateral flow, are still modeled with daily time-step. The output of these  
61 processes modeled at daily time-step is then distributed equally at the sub-hourly time-step. This

62 improved SWAT model has been used to perform sub-daily rainfall-runoff simulations (Boithias  
63 et al., 2017). Ficchi et al., (2016) modeled streamflow using a four-parameter lumped GR4  
64 (modified from GR4J, which stands for modèle du Génie Rural à 4 paramètres Journalier) model  
65 at different time-steps ranging from 6 min to 1 day, and studied the impact of frequency on  
66 model performance. However, their study did not model continuous streamflow, rather they  
67 simulated individual storm events. Their study found a mixed model response, i.e., both increase  
68 (0.7 to 0.8) and decrease (0.8 to 0.69) in Kling Gupta Efficiency (Gupta et al., 2009) for model  
69 with increases in temporal resolution. Temporal resolution of input data also affects simulation  
70 results in a catchment model. Numerous studies have shown that the use of input data with  
71 higher temporal frequency improves model accuracy (Huang et al., 2019; Wang et al., 2009;  
72 Pang et al., 2018). On the other hand, simulating model output at a shorter time-step causes a  
73 reduction in model accuracy (Gassman et al., 2007; Boithias et al., 2017; Bressiani et al., 2015).

74 A data-driven model is considered as an alternative approach to overcome these  
75 complexities, and such models have higher predictive accuracy (Pascual et al., 2013; Park et al.,  
76 2019). Numerous studies have been conducted to simulate hydrological processes using neural  
77 networks (NNs), which is one of the popular types of data-driven models (Ilunga and Stephenson,  
78 2005; Ogwueleka and Ogwueleka, 2009). Several review papers (Besaw et al., 2010; Yaseen et  
79 al., 2015; Mosavi et al., 2018) have shown that most data-driven rainfall-runoff models have  
80 used daily time-steps and very few studies have been conducted using an hourly time-step. No  
81 study mentioned in these reviews showed any data-driven model using sub-hourly time-step for  
82 continuous streamflow prediction or estimating both surface and sub-surface outflows  
83 simultaneously. Granata et al., (2016) also employed a machine learning methodology for sub-

84 hourly streamflow simulation. However, this study focused only on individual hydrographs and  
85 not on continuous streamflow prediction.

86 Long short-term memory (LSTM) cell constitute a special type of NN, which has also  
87 been used for streamflow simulation (Kratzert et al., 2018; Le et al., 2019; Yan et al., 2019;  
88 Campos et al., 2019). The special feature of LSTM is its ability to learn time-dependent features  
89 using its “memory” thereby it is regarded as an adequate NN for modeling hydrological cycles  
90 (Shen, 2018; Greff et al., 2016; Zhang et al., 2018). To the best of our knowledge, no studies  
91 have been published so far that discuss the use of LSTMs to simulate surface and sub-surface  
92 flow simultaneously at a sub-hourly time-step. However, such a study is required because  
93 modeling hydrological response of catchments at minutes-scale temporal resolution can enhance  
94 the capacity of hydrological models to simulate contaminants whose concentrations vary at  
95 logarithmic scale within short span of time such as fecal bacteria. In this study, we developed  
96 two different data-driven models based on LSTM neural networks and compared their  
97 performance with a physical model (HSPF) using sub-hourly data collected at the outlet of a  
98 highly responsive headwater catchment in northern Laos, where land use dramatically changed  
99 over the past 20 year: annual crops was replaced by teak tree plantations managed without  
100 understorey. As different landuses have different flow patterns, change in landuse can affect soil  
101 loss or stream water quality (Ribolzi et al., 2017). The specific objectives of this study were (1)  
102 to evaluate the models’ ability to perform simulations of surface runoff and sub-surface flow at  
103 high temporal resolution of 6 minutes, (2) to conduct sensitivity analysis of the models  
104 developed in this study, and (3) to predict HRU level surface and sub-surface responses from  
105 LSTM-based models and to analyze whether HRU-level discretization in LSTM-based model  
106 can yield better result as compared to non-HRU based LSTM model.

## 107 **2 Materials and Methods**

### 108 **2.1 Study area**

109           This study was conducted in a 0.6 km<sup>2</sup> Houay Pano headwater catchment, located 10 km  
110 south of Luang Prabang city in Northern Lao P.D.R. It is a sub-basin of the Houay Xon river  
111 basin, which is a tributary of the Mekong River (**Figure 1**). The experimental site is part of the  
112 critical zone observatories' network named Multiscale TROPICAL CatchmentS (M-TROPICS),  
113 which belongs to the French Research Infrastructure OZCAR (Gaillardet et al., 2018). This  
114 catchment can be considered as being representative of the montane agro-ecosystems of South-  
115 East Asia. The bedrock is made up of siltstone and fine-grained sandstones of Permian to upper  
116 carboniferous age. Soils are Entisol, Ultisol, and Alfisol covering 20, 30, and 50% of the  
117 catchment, respectively (Chaplot et al., 2005). The slope in the area varies from 0% to 171%  
118 with an average slope of 54% (Ribolzi et al., 2016). The climate is sub-tropical humid. The mean  
119 annual rainfall is 1500 mm per year; however, the rainfall pattern is highly seasonal as the  
120 monsoon season, which runs from mid-May to mid-October, constitutes 77% of the rainfall. The  
121 average monthly temperature at the site lies between 12 and 35 °C with the highest temperature  
122 in April, just at the beginning of the wet season. The humidity level varies from 17% to 100%.  
123 The catchment experiences several storms during the rainy season, with heavy rainfall (up to 100  
124 mm h<sup>-1</sup>), a phenomenon which is characteristic of tropical regions (Ribolzi et al., 2016). We  
125 measured hourly temperature (Celsius), relative humidity (%), wind speed (m/s), and solar  
126 radiation (J/m<sup>2</sup>). The precipitation, electrical conductivity of stream water, surface and sub-  
127 surface flow were measured at 6-minute time-step at the study site. Moreover, a survey is

128 conducted every year to ascertain landuse changes in study area. More details on data acquisition  
129 are given in Supplementary Information (**Text S1**).

130 The area consists of four major land use types consisting of annual crops, teak, fallow,  
131 and forests (**Figure S1**). Recently, the area has undergone major land use changes with an  
132 increasing number of teak tree plantations ([Ribolzi et al., 2017](#)). Several studies have been  
133 conducted to understand the impact of land use changes on hydrological responses in the area  
134 ([Ribolzi et al., 2018](#); [Patin et al., 2018](#); [Kim et al., 2018](#)). We observed that the increase in teak  
135 tree plantations from 2002 onwards has resulted in a decrease of infiltration and consequently an  
136 increase in overland flow and sediment yield ([Ribolzi et al., 2017](#)).

## 137 **2.2 Hydrological Simulation Program-FORTRAN Model setup**

138 Hydrological Simulation Program-FORTRAN (HSPF) is a lumped model for water  
139 quality and quantity modeling at catchment scale developed during the 1970s ([Johanson and](#)  
140 [Davis, 1980](#)). The steps used to build the HSPF model are summarized in **Figure 2(a)**. We used  
141 BASINS 4.1 ([Kinerson et al., 2009](#)) software to prepare the input file for HSPF. This software  
142 pre-processes land use shapefiles, digital elevation models (DEM), and timeseries data of  
143 environmental variables such as precipitation, evapotranspiration, and temperature to prepare an  
144 input file for HSPF. Post processing steps were carried out on the input file and input data to  
145 incorporate the impact of changing land use, details of which are given in the Supplementary  
146 Information (**Text S2**). Furthermore, we performed Morris OAT ([Morris, 1991](#)) sensitivity  
147 analysis to find out the most sensitive parameters for the model. We chose 13 parameters for  
148 each of the four land uses present in the study area for sensitivity analysis (**Table S1**). Thus, the  
149 total number of parameters chosen for sensitivity analysis were 52. These 52 parameters are used



150 in equations which control the movement of water on pervious land segments in HSPF. Details  
151 on the implementation of the sensitivity analysis can be found in the Supplementary Information  
152 (**Text S3**). After sensitivity analysis, we calibrated the model by reducing the mean square error  
153 (MSE) between observed and predicted outflows, which was calculated using the following  
154 equation:

$$155 \quad MSE = \frac{[\sum_{i=1}^n (o_i - p_i)^2]}{n} \quad (1)$$

156 where  $p_i$  and  $o_i$  are simulated and observed data, respectively, and  $n$  represents the number of  
157 points in the data set. We used a truncated Newton algorithm (Nash, 1984) provided by the  
158 Python library ‘scipy’ (Jones et al., 2001) to minimize the loss function.

### 159 **2.3 Long Short-Term Memory (LSTM)**

160 Neural networks (NN) are a group of algorithms which work similar to how the human  
161 neural system is thought to work and are used to recognize patterns (Fukushima, 1980). They  
162 consist of a stack of layers of neurons where each neuron is associated with weights and  
163 activations. NNs can be calibrated to learn a non-linear function through backpropagation, in  
164 which the weights and biases in each layer of the NN are optimized by reducing the error/loss  
165 between observed and predicted output from the network (Rumelhart et al., 1988). The calibrated  
166 network, which is commonly known as a trained network, is then used to predict output from  
167 unseen data during validation (Rumelhart et al., 1988). Such models based on NNs are also  
168 considered as black-box models, where we only deal with input and output while the model itself  
169 finds relationships between the input and output data (Benítez et al., 1997). Recurrent Neural  
170 Networks (RNN) are a special kind of neural networks which are designed to work with time-

171 series data because of their ability to capture long term temporal dependencies in data  
 172 (Rumelhart et al., 1988). Simple RNNs suffer from the problem of vanishing gradient in deep  
 173 neural networks where they fail to capture long range dependencies (Hochreiter, 1998).

174 One solution to this problem is known as the Gated Recurrent Unit (GRU) and was  
 175 proposed by Cho et al., (2014). They introduced the concept of gates which control the flow of  
 176 information within the recurrent unit. Another solution to the problem of vanishing gradient was  
 177 proposed by Hochreiter and Schmidhuber, (1997) which is known as long short-term memory  
 178 (LSTM). LSTM uses three gates namely forget, update and output gates to control the flow of  
 179 information. The current candidate cell state  $C_c^{<t>}$  depends on previous activation. The current  
 180 cell state  $C^{<t>}$  is calculated using update and forget gate and then the output gate is used to  
 181 decide the activations at current time step.

$$C_c^{<t>} = \tanh(W_c [a^{<t-1>}, x^{<t>}] + b_c) \quad (2)$$

$$\Gamma_f = \sigma(W_f [c^{<t-1>}, x^{<t>}] + b_f) \quad (3)$$

$$\Gamma_o = \sigma(W_o [c^{<t-1>}, x^{<t>}] + b_o) \quad (4)$$

$$\Gamma_u = \sigma(W_u [c^{<t-1>}, x^{<t>}] + b_u) \quad (5)$$

$$c^{<t>} = \Gamma_u * C_c^{<t>} + \Gamma_f * c^{<t-1>} \quad (6)$$

$$a^{<t>} = \Gamma_o * \tanh c^{<t>} \quad (7)$$

182

183 In these equations, W and b are weights and biases whose values are calibrated when the  
 184 model is trained. The model is fed with inputs x at time-step t and the activation at time-step t  
 185 which is calculated using (Eq. 7) is taken as the output. In rainfall-runoff modeling, model output  
 186 has strong time dependence. There is time delay in the stream response to precipitation (Talei  
 187 and Chua, 2012) and this lag time depends on catchment features (Singh, 1988). LSTMs have the

188 ability to learn this behavior because of their ability to learn patterns in time-series data (Lin Hsu  
189 et al., 1997). In this study, we developed two NN-based models. The steps to develop a simple  
190 LSTM model are briefly described in **Figure 2(b)** while the steps for a detailed, more complex,  
191 HRU-based LSTM model are summarized in **Figure 2(c)**.

192

### 193 **2.3.1 Setup for simple LSTM model**

194 The simple LSTM model (**Figure 2(b)**) consists of only a single LSTM layer. We chose  
195 the parameters to build this NN based on a trial and error procedure. This simple LSTM model is  
196 considered our baseline model and was used to compare the performance of the HRU-based  
197 LSTM model. The LSTM layer takes all input data and is calibrated to produce two outputs  
198 which are considered representative of surface and sub-surface flow (**Figure 3**). Although the  
199 same LSTM layer generates two outputs, it does not know which one is surface and which one is  
200 sub-surface flow. However, this distinction is made by comparing one (first) output of the model  
201 with observed surface flow and the second output of model with sub-surface flow. This  
202 comparison is done by calculating the MSE and then the model adjusts the weights and biases of  
203 the LSTM layer by back propagation in such a way that it tries to reduce the value of the MSE.  
204 In this way, the model learns implicitly that its first output must correspond to surface flow and  
205 the second output has to correspond to sub-surface flow.

### 206 **2.3.2 Setup for HRU-based LSTM model**

207 The second structure of LSTM model is the HRU-based structure consisting of 36  
208 parallel NNs (**Figure 4**). Each of these parallel networks is similar to a simple LSTM structure,  
209 however, it represents one hydrological response unit (HRU) instead of the whole catchment.

210 Each parallel NN consists of layered LSTM cells with 128 hidden units. We chose the number of  
211 hidden units based upon hyper-parameter optimization results. The input to LSTM at each time step  
212 consists of a 2-dimensional array of shape (sequence length, input features). The sequence length and  
213 input features are given in **Table 1**. The output from LSTM at each time step is equal to the number of  
214 hidden units. A fully connected layer was used to convert the output from LSTM into the specific  
215 dimension. However, the multiple fully connected layer can increase computation time as well as the  
216 model complexity. In order to avoid this, we used a single fully connected layer instead of a deep neural  
217 network after LSTM. Several studies also showed a single fully connected layers for developing  
218 hydrological models (Kratzert et al., 2018; Zhang et al., 2018; Kratzert et al., 2019; Kratzert et al., 2019b;  
219 Li et al., 2020). The fully connected layer in this study generates two outputs: surface runoff and sub-  
220 surface flow (**Figure 3**) within an HRU. The number of layers in each of the parallel NN and the  
221 number of hidden units were decided by hyper-parameter optimization and are given in **Table 1**.

222 An HRU is defined here as a distinguished land use in a distinguished sub-basin. This  
223 means land uses present in different sub-basins were considered as separate HRUs. This is  
224 different from HSPF where similar land uses in different sub-basis are considered are merged  
225 into one HRU. Thus, if a land use type, e.g. grass, is present in a catchment with 9 sub-basins  
226 and all the sub-basins have this type of land use, we will have 9 HRUs for this land use and nine  
227 separate NNs are assigned to simulate processes in these HRUs. Similarly, if a ‘forest’ land use  
228 is present in 5 sub-basins in the catchment, this will result in 5 other HRUs in the model. This is  
229 further illustrated in **Figure S2** where a catchment consists of 5 sub-basins (A, B, C, D, E) and  
230 four land use types (i, ii, iii, iv) and 15 HRUs.

231 Each of the parallel NNs in **Figure 4** shares HRU-invariant input data such as solar  
232 radiation, air temperature, etc. The HRU-specific input data, such as precipitation received by

233 each HRU, was also prepared and was fed only to the corresponding NNs. The environmental  
234 data, such as air temperature and solar radiation, is experienced equally by the whole area of the  
235 catchment. Thus, all NNs share this environmental data. On the other hand, parameters which  
236 depend on HRU characteristics, such as its area and distance to the outlet, were calculated for  
237 each HRU. These HRU-specific parameters were only fed to the NNs representing the  
238 corresponding HRUs in the model. Precipitation data was measured for the whole catchment,  
239 and then precipitation received by each HRU was calculated based on the area of that HRU. This  
240 HRU-specific data can be viewed in **Figure S7** and **Figure S8**.

241 As the land use in the study area varies with time, this implies that the locations of HRUs  
242 also vary with time. Thus, all the HRU-specific data, i.e., distance to outlet, area, and volume of  
243 precipitation received, was also calculated accordingly. This time-varying HRU-specific data can  
244 be viewed in **Figure S7** and **Figure S8**. One implication of this is that we considered all possible  
245 HRUs in the study area. For example, if the land use ‘grass’ is not present in sub-basin 1 in year  
246 2011, it may appear in 2012 and then disappear again. Thus, we considered the HRU ‘grass in  
247 sub-basin 1’ for the whole simulation period, though the input values for year 2011 and 2013  
248 will be zeros in this case.

249 The catchment area consisted of 9 sub-basins and 4 types of land uses, thus implying 36  
250 possible HRUs. As the land use inside a sub-basin is distributed and no specific distance from an  
251 HRU to the catchment outlet can be measured, we used the distance of the sub-basin from the  
252 outlet as representative of all land uses inside that sub-basin. This means all the land uses/HRUs  
253 inside a sub-basin were considered to have the same distance from the outlet as that sub-basin.

254 This generalization results in certain HRUs having the same distance from the outlet, however, it  
255 still maintains HRU-specific information.

256 Each of the parallel NNs in **Figure 4** produces two outputs which are considered as  
257 representative of HRU-specific surface and sub-surface flow. Corresponding values of surface  
258 and sub-surface flow are added in cumulative order. This order of addition is the same as the  
259 stream filling order in the catchment. This cumulative and ordered filling of outputs is similar to  
260 realistic stream routing. The final values of surface and sub-surface flow are considered as model  
261 outputs and are compared with observed values to calculate the mean square error using  
262 Equation 1.

263 This structure allows us to build a detailed model of the catchment, where outflow from  
264 each land use is simulated separately and instead of one value of total streamflow, the surface  
265 and subsurface outflow from the catchment are simulated. More details on the implementation of  
266 this NN in the computer program are given in **Text S4** of the Supplementary Information. The  
267 motivation for HRU-based LSTM model was drawn from physically based models such as  
268 SWAT or HSPF where the study area is discretized into smaller HRUs. All processes are  
269 modeled at HRU level in these models. In order to compare results of LSTM-based model with  
270 HSPF, the study area was discretized into HRUs. Another purpose of discretizing study area for  
271 HRU-based LSTM was to assess the impact of increase in spatial resolution on model  
272 performance.

### 273 **2.3.3 Hyper-parameter optimization (HPO) based on window size**

274 The performance of a NN model is mainly governed by a set of parameters, which are  
275 used to build the NN, such as length of input data fed to it at each time-step, and number of

276 nodes in a layer (Hutter et al., 2015). These parameters are called hyper-parameters and their  
277 description and possible ranges are presented in **Table S3**. To achieve the best performance with  
278 calibration, we need to optimize these parameters, because a slight change in any of these  
279 parameters can worsen or improve the performance of the model. Different derivative free  
280 optimization algorithms are those which aim to solve problems given as black box (Lakhmiri et  
281 al., 2019). Direct search and Bayesian are one of such methods. Direct search is an ‘a priori’  
282 method where the decision maker articulates preferences before optimization. Bayesian  
283 optimization is one of ‘a posteriori’ methods which aims to generate a representative set of  
284 pareto optimal solutions and then the best among them is chosen (Chen and Li, 2018). We  
285 selected Bayesian optimization approach because of it being a popular approach to optimize  
286 hyper-parameters in machine learning models (Shahriari et al., 2015; Snoek et al., 2015; Frazier,  
287 2018). The details about implementation of Bayesian optimization are given in **Text S5**.

288         Several open source libraries are available for implementing Bayesian optimization  
289 method in Python programming language such as Hyperopt (Bergstra et al., 2015) and scikit-  
290 optimize (Kumar and Head, 2017). We used scikit-optimize library because it allows the use of  
291 Gaussian Processes as surrogate function. Implementation of Bayesian in Hyperopt can be done  
292 by making use of Tree Parzen Estimator (Bergstra et al., 2011). The advantage of Gaussian  
293 Processes is that it can consider the interaction between hyper-parameters during the  
294 optimization (Dewancker et al., 2015). The surrogate function is the probability model of  
295 objection function and it calculates the probability of loss with respect of input values. In  
296 Bayesian optimization method, this surrogate function is optimized instead of actual objective  
297 function. The methodology of selecting the new parameter from parameter space was ‘Expected  
298 Improvement’ to the surrogate function. The expected improvement algorithm (Mockus,1975;

299 [Jones et al., 1998](#)) considers the size of the improvement. We used default parameters used by  
 300 scikit-optimize ([Kumar and Head, 2017](#)) library in using Gaussian Processes. These parameters  
 301 include ‘optimizer’, ‘kaapa’ and ‘xi’ and are described in following sentences. The ‘optimizer’  
 302 minimizes the acquisition function. We used Limited-Memory Broyden-Fletcher-Goldfarb-  
 303 Shanno ([Andrew and Gao, 2002](#)) as optimizer. The parameter ‘kappa’ controls variance in  
 304 predicted values and was set to 1.96. The parameter ‘xi’, determines how much improvement  
 305 should be taken into consideration over previous best values and was set to 0.01.

306 The computation time of HPO depends upon the number of epochs to train a single model and the  
 307 number of iterations used for optimization. Furthermore, it also depends upon the complexity of model  
 308 being built at a specific iteration. The computation time, in general, increased by increasing the sequence  
 309 length. We performed 50 iterations for each sequence length (**Figure S5**). The model was trained for 100  
 310 epochs during each of these iterations. The computation time taken for optimizing hyper-parameters was  
 311 15, 19, 25, 40 and 45 hours for sequence lengths of 20, 30, 40, 50 and 60, respectively. Although HPO  
 312 needs considerable computation power, this method can improve the model performance by finding the  
 313 optimal hyperparameter set. The model performance depending on the iteration is showed in **Figure S5**.

#### 314 **2.4 Performance metrics and data splitting**

315 The performance of each model was evaluated using Nash-Sutcliffe Efficiency (NSE),  
 316 mean squared error (MSE) and percentage bias (PBIAS). The MSE was calculated according to  
 317 equation 1 and the equation used to calculate NSE and PBIAS are:

$$318 \quad \text{NSE} = 1 - \frac{\sum(p_i - o_i)^2}{\sum(o_i - \bar{o})^2} \quad (8)$$

$$319 \quad \text{PBIAS} = \frac{\sum_{i=1}^n O_i - p_i}{\sum_{i=1}^n O_i} \times 100 \quad (9)$$



320 where  $p_i$  is simulated data,  $o_i$  is observed data, and  $n$  is the number of points in the data  
321 set. Values of MSE indicate how closely the predictions follow the observed values. In model  
322 training, 70% of the input data corresponding from January 2011 to January 2013 was applied.  
323 15% of the data were used as validation and test, respectively. All three models produced two  
324 outputs—surface and sub-surface flow—and during optimization of parameters, an average error  
325 of the surface and sub-surface flow was calculated. This averaged error was then considered as  
326 the objective function which each model tries to minimize. Predicted total discharge is thus the  
327 sum of surface and sub-surface flows in each case.

328 In order to avoid overfitting in LSTM based models, we used a mild regularization  
329 technique, namely early stopping ([Goodfellow et al., 2016](#)). We checked the performance of the  
330 models after each epoch on validation data. The model had not processed this data during  
331 calibration. We stopped calibrating the model when validation loss reached a plateau even if  
332 calibration loss kept on decreasing.

### 333 **3. Results**

#### 334 **3.1 HSPF Results**

##### 335 **3.1.1 Sensitivity Analysis**

336 We carried out sensitivity analysis for sub-surface flow and total discharge separately.  
337 Based on the results of sensitivity analysis, we selected 12 parameters for baseflow and for total  
338 discharge which had the strongest impact on these outflows for calibration. Not all parameters  
339 for baseflow and total discharge are different, rather there are some common parameters which  
340 had a strong impact on both sub-surface flow and total discharge (**Table 2**). Both sub-surface

341 flow and total discharge were highly sensitive to INFILT, which describes infiltration capacity  
342 (Bicknell et al., 2001), while only sub-surface flow was sensitive to AGWETP, Basetp, and  
343 DEEPFR.

344 The parameters AGWETP and Basetp control the amount of evapotranspiration that  
345 can be taken from active groundwater storage and baseflow, respectively (Bicknell et al., 2001).  
346 As the definitions of these two variables suggest, they are closely associated with baseflow. Thus,  
347 sensitivity analysis showed these parameters to be more important for sub-surface flow, which is  
348 the sum of groundwater flow and interflow. These results are consistent with the similar studies  
349 (Xie and Lian, 2013; Baek et al., 2017; Diaz-Ramirez et al., 2013), which also demonstrated that  
350 INTFW, IFILT, DEEPFR, and AGWETP are among the most important parameters for  
351 streamflow.

### 352 3.1.2 Estimation of surface and sub-surface flow using HSPF

353 Figure 5 and Figure 6 shows predictions from the HSPF model for the calibration,  
354 validation and test periods. We evaluated the performance of the model by measuring the MSE  
355 and NSE for the calibration and test periods separately. Values of these errors for surface, sub-  
356 surface, and total flow are given in Table 3. The predicted sub-surface flow in Figure 5 and  
357 Figure 6 is often underestimated, while the surface flow simulated by HSPF is mostly  
358 overestimated. This is the reason there is large positive PBIAS for surface flow and large  
359 negative PBIAS for sub-surface flow (Table 3). Although the predicted sub-surface flow is very  
360 low, the predicted total discharge is higher. The predicted total discharge is higher because of the  
361 large amount of input in the form of surface runoff. Overestimation of surface flow and under-  
362 estimation of sub-surface flow was also observed by Hoang et al., (2014) after the application of

363 the SWAT model to a watershed in Denmark. This research attributed this behavior to the  
364 inadequacy of the model structure for simulating these processes.

365 UZSN represents the storage capacity of the upper zone in the HSPF model (Bicknell et  
366 al., 2001), which is a soil zone (Table 2). A higher value of UZSN means that the soil has a  
367 higher storage capacity and thus more water will be retained in the upper zone which becomes  
368 available for evapotranspiration (Bicknell et al., 2001). Our calibrated UZSN values are closer to  
369 the upper limits, which means more water is being retained in the soil zone, eventually leading to  
370 higher evapotranspiration. In other words, this means more water is available for  
371 evapotranspiration from upper zone.

372 We observed that predicted sub-surface flow was higher in 2013 as compared to 2011,  
373 while it was the lowest in 2012. We observed this trend because of changes in land use during  
374 these years (Figure S9). The rise of sub-surface flow in 2013 can be attributed to an increase in  
375 fallow land use and a decrease in annual crop land use in 2013. A recent study by Ribolzi et al.,  
376 (2017) found a correlation between higher sub-surface flow and the increase in teak plantations  
377 in this catchments. Although teak and annual crop land use result in higher surface flow, the joint  
378 contribution of teak and annual crop decreased in 2013 and the contribution of fallow land use  
379 increased. The smaller sub-surface flow observed during 2012 could be due to the relatively  
380 higher teak and annual crop land use during this year as compared to other years.

## 381 **3.2 Estimation of surface and sub-surface flow using deep learning**

### 382 **3.2.1 Simple LSTM**

383 The simple LSTM model consisted of a single LSTM layer and was built using the  
384 hyper-parameters given in Table 1. We then used the model calibrated with these hyper-

385 parameters for evaluation during the test period. The performance of the model during  
386 calibration and test for surface, sub-surface, and total flow can be seen in **Figure 7**, **Figure 8** and  
387 **Table 3**.

388 The NSE values for surface runoff prediction during calibration and test were 0.43 and  
389 0.64, respectively. These NSE values categorize the model performance ‘unsatisfactory’ and  
390 ‘satisfactory’ according to [Moriassi et al., \(2015\)](#). However, PBIAS, which measures average  
391 tendency of model to predict flow larger or smaller than observed is mostly between ‘very good’  
392 (-3.2) and ‘good’ (-5.6) (**Table 3**). Despite this, the model captured most of the peaks in surface  
393 runoff during both the calibration and test periods. However, the predicted peaks are mostly  
394 lower than the observed peaks. This discrepancy can be attributed to the use of MSE for model  
395 calibration because MSE focused to reduce the average error between observation and simulation.  
396 The inability of model to capture peaks is also evident from flow duration curves for surface,  
397 sub-surface and total discharge (**Figure S13**). The percentage exceedance of predicted flows is  
398 below the observed in areas of high flows (**Figure S13**). For sub-surface flow, this model  
399 predicted almost all the peaks yet failed to follow the trend of rising and falling limbs, which  
400 resulted in lower NSE values. Another important aspect of simple LSTM model is its ability to  
401 perform better for surface runoff as compared to sub-surface runoff. This is evident from Table 3,  
402 which shows all performance metrics for surface runoff better than those of sub-surface flow.

### 403 **3.2.2 HRU-based LSTM model**

404 We built the HRU-based LSTM model using information obtained from HPO. We used  
405 information about the activation function, normalization, and loss calculation methods and cell  
406 type from HPO. The choice of activation function affects the kind of non-linearity applied.  
407 Options for the loss calculation method were ‘normal’ or ‘weighted’. In the weighted loss

408 calculation method, the loss value is more sensitive to peak flows. The choices for cell type, in  
409 order to build NN, were GRU and LSTM. The HPO was then allowed to decide which of these  
410 two cells perform best. The HPO algorithm varied the values of these hyper-parameters during  
411 the optimization process until it found the best combination of hyper-parameters. This  
412 optimization was performed for five different sequence lengths. **Figure S5** shows the results of  
413 optimization, where the plot for each sequence length indicates how the loss value was reduced.  
414 It shows how the optimization algorithm attempted to obtain the best hyper-parameters for a  
415 specific sequence length. **Table 4** enlists configuration of models which resulted in maximum  
416 reduction in loss value for each sequence length. It can be seen that the best HPO results were  
417 mostly obtained using a rectified linear unit (ReLU), performing normalization of input data  
418 before using it, using an LSTM cell instead of a GRU cell, and using the weighted loss  
419 calculation method (**Table 4**). The values of sequence length and batch size were not optimized  
420 using HPO because increasing them is equivalent to increasing the amount of input data being  
421 fed to the NN. This exponentially increases the amount of computation, which requires greater  
422 processing and memory resources. In this regard, we used a trial and error method to obtain  
423 better optimum values for other hyper-parameters such as sequence length, batch size, etc. The  
424 optimized set of hyper-parameters which were used to build the HRU-based LSTM model are  
425 given in **Table 1**.

426 Plots for surface, sub-surface, and total flow for calibration, validation and test data are  
427 shown in **Figure 9** and **Figure 10** respectively. The performance metrics obtained for this model  
428 are given in **Table 3**. We observed underestimation of surface runoff, which is similar to what  
429 we observed in predicted surface runoff from the simple LSTM model. However, in this case  
430 there was more under estimation as compared to the simple LSTM. This is the reason that the

431 MSE value, which is the average error for the whole simulation range, was higher during  
432 calibration and test as compared to the MSE value of the simple LSTM model. The NSE values,  
433 which measure the accuracy of prediction, were 0.66 and 0.63 for calibration and test of sub-  
434 surface flow, respectively, which makes the model performance ‘satisfactory’ (Moriassi et al.,  
435 2015).

## 436 4. Discussion

### 437 4.1 Overall comparison of three models

438 By comparing the MSE and NSE values of all three models from **Table 3**, we can  
439 conclude that the simple model performed better for surface flow prediction. The simple LSTM  
440 model showed an NSE value of 0.64 and MSE value of  $8.3\text{-}5\text{ m}^3\text{s}^{-1}$  for surface runoff prediction,  
441 which are the best values obtained among all three models. Although the simple LSTM model  
442 was meant to serve as a baseline model, the more complex HRU-based LSTM model could not  
443 perform better for surface flow prediction. It is interesting to note that in this case, increasing  
444 model complexity has not resulted in improved model performance. It has already been reported  
445 that adding complexity to an NN does not necessarily imply that it will outperform its simpler  
446 counterpart (Makridakis et al., 2018).

447 Overall performance of all models range from satisfactory to not-satisfactory as per  
448 criteria set by Moriassi et al., (2015). One of reasons for this lower accuracy can be attributed to a  
449 finer time-step of simulation. Indeed, several studies have reported deterioration in model  
450 performance for streamflow estimation with increase in simulation time-step (Stern et al., 2016;  
451 Gassman et al., 2007), especially in smaller catchments (Spruill et al., 2000). In an extensive  
452 review of over 100 SWAT applications in Brazil. Bressiani et al., (2015) found that only 6% of

453 studies with monthly simulations resulted in NSE values of less than 0.5. On the other hand,  
454 when daily time-step was used, 25% of studies rendered NSE value below 0.5. [Boithias et al.,](#)  
455 [\(2017\)](#) reported degradation of validation NSE from 0.66 to 0.49 when streamflow was first  
456 simulated at a daily time-step and then at an hourly time-step. The reason for lower accuracy at  
457 shorter time-steps can be the use of sparsely distributed rainfall gauges which are unable to  
458 capture the spatial details of rainfall inputs ([Gassman et al., 2007](#)). Similarly, another explanation  
459 for higher model accuracy when using longer time-steps is that longer time-steps integrate the  
460 variability at smaller time-steps ([Boithias et al., 2017](#)).

461 For sub-surface flow, although the HSPF model performed best in terms of NSE, the  
462 predicted sub-surface flow was much lower than the observed sub-surface flow. The sub-surface  
463 flow predicted by HSPF in **Figure 5** and **Figure 6** , is much lower than the observed flow. This  
464 is the reason we see large negative values of PBIAS from the flow duration curves for predicted  
465 sub-surface flow is much below the observed (**Figure S12**). The simple LSTM model was able  
466 to predict most of the peaks for sub-surface flow, however the value of NSE is lower as  
467 compared to that of the HRU-based LSTM model. The better values of NSE for sub-surface flow  
468 from the HRU-based LSTM model can be attributed to the better prediction of recession in peaks.  
469 The slopes in the falling limbs of predicted peaks from the HRU-based LSTM model in **Figure**  
470 **S10**, which are absent in the peaks predicted by the simple LSTM model. If we consider MSE  
471 values, the HRU-based LSTM model outperformed HSPF for both surface flow as well as sub-  
472 surface flow during calibration period.

473 In all models, the predicted flow peaks were lower than the observed peaks for both  
474 surface and sub-surface flow, except the predicted surface flow from HSPF. However, in HSPF,

475 the number of predicted storm events were much more than the observed, which resulted in a  
476 negative NSE value. In the case of the HRU-based LSTM model, although it predicted most of  
477 the storm events, it still under-predicted surface flow.

478 The discrepancy between train and test MSE was caused by the difference in data  
479 distribution during these periods. The train data set had larger standard deviation than the  
480 validation and test data set (Table S4). The dataset with larger variance can have large MSE  
481 (Munna et al., 2015; Grams et al., 2002). If the training performance of a model is significantly  
482 larger than that of test data, this indicates overfitting. On the other hand, better performance for  
483 test data set in our case indicates different distribution of training and test data sets.

484

#### 485 **4.2 Advantages and Limitations of HSPF**

486 As the HSPF is a process driven model, thus simulations resulting from it give insights  
487 about behavior and condition of catchment. The higher values of a variable such as UZSN  
488 translate into large storage potential in upper zone of soil. However, simulation results from  
489 HSPF are greatly influenced by calculated potential evapotranspiration which itself can vary  
490 based on the method of evapotranspiration calculation used. Our HSPF results showed that major  
491 portion of the rainfall is evapotranspired. In the HSPF model, the amount of actual  
492 evapotranspiration is increased until the requirement created by the potential evapotranspiration  
493 is satisfied. If potential evapotranspiration is very high, the model allows more available water  
494 from storage to return to the environment as actual evapotranspiration. In our simulations, lower  
495 predicted flows from the HSPF model may also be due to the overestimation of potential  
496 evapotranspiration (Table S2) as has been the case in the studies of Yeh, (2017) and



497 [Prudhomme and Williamson, \(2013\)](#). In this study, we calculated daily evapotranspiration and  
498 then distributed to 6 min by calculating daily sunshine hours. This interpolation of daily  
499 evapotranspiration to 6-min time-step can also be a reason of poor HSPF performance. There  
500 have been several studies showing that using evapotranspiration values calculated at a higher  
501 temporal resolution results in better model performance ([Debele et al., 2009](#)). The conceptual  
502 physically-based models can render poor performance if one of the model variable is incorrectly  
503 calculated. [Ouellet-Proulx et al., \(2019\)](#) compared the performance of five different ET and  
504 evaporation models for rainfall-runoff modeling and showed that the choice of ET model affects  
505 streamflow by 3 to 24 percent. On the other hand, the deep learning models are less likely to  
506 suffer from these errors because they are not explicitly process driven.

#### 507 **4.3 Advantages of LSTM model**

508 One of the key characteristics in surface runoff simulations is the lag time between  
509 rainfall and surface runoff ([Talei and Chua, 2012](#)). The lag time between observed surface runoff  
510 and incoming rainfall for two storm events of September 2013 can be seen in **Figure S11**. This  
511 figure also compares the results of lag time for all three models. These storm events are in the  
512 test period; thus this figure is a good representation of the ability of models to simulate lag time.  
513 It can be observed in the figure that HSPF predicts surface runoff as soon as there is a rainfall  
514 event while both our NN models show a lag time. Although the peaks predicted by the HRU-  
515 based LSTM model are lower than those predicted by the other models, the model showed  
516 responses to both storm events with lag time.

517 The simple LSTM model takes much less computing time as compared to the HRU-based  
518 LSTM model. This is self-evident because the HRU-based LSTM model has 36 times more

519 parameters to calibrate as compared to the simple model. The number of calibration parameters  
520 for each NN model can be calculated from the hyper-parameters given in **Table 1**. For the simple  
521 LSTM model there were 258 parameters to calibrate (128 weights and biases for an LSTM with  
522 128 hidden units and one weight and bias for the fully connected layer). Similarly, the number of  
523 parameters calibrated by the HRU-based LSTM model were 9,288. The computation time of  
524 HRU-based LSTM model did not scale with number of parameters. We observed an average  
525 time of 4 minutes per epoch for HRU-based LSTM while 0.5 minutes per epoch for simple  
526 LSTM model. We used Intel® Core™ i7-8700 processor with graphic card of NVIDIA GeForce  
527 GTX 1060 having 6 Gigabytes of dedicated GPU memory along with 32 Gigabytes of Random-  
528 Access Memory. The parallel computing power of Tensorflow ([Abadi et al., 2016](#)) prevented the  
529 scaling of training time with model parameters ([Adie et al. \(2018\)](#)). The total training time  
530 however depends upon the number of training epochs used. The HRU-based LSTM model took  
531 262 minutes for 66 epochs while it took approximately 100 minutes for simple LSTM to train for  
532 214 epochs.

533         The results of the LSTM-based models show that total streamflow was mainly governed  
534 by sub-surface flow while the surface flow only contributed to flood peaks during rainfall events.  
535 It can be observed that the predicted flow patterns for sub-surface flow and total discharge are  
536 the same, except for peak heights (**Figure 7 to Figure 10**). The peaks are higher in total  
537 discharge, which means that surface flow only contributes to increases in peak heights. This can  
538 also be seen in flow duration curves for all three models (**Figure S12, S13 and S14**) where the  
539 predicted flow duration curve is always below observed in high flow regions. This result is  
540 consistent with a previous study within Houay Pano catchment that showed the larger  
541 contribution of baseflow to streamflow during floods ([Ribolzi et al., 2018](#)). In our study, the total

542 surface and sub-surface flow from simple LSTM model was 78 and 2,160 mm. Similarly, the  
543 HRU-based LSTM model also showed dominance of sub-surface flow in the catchment. The  
544 total simulated surface and sub-surface flow for three years using HRU-based LSTM model was  
545 32 and 1,913 mm respectively. The large gap between two values is because of absence of  
546 surface runoff during most of the days in year when there is no rainfall.

547 Under-estimation of peak flows using lumped, physically-based models is a frequent  
548 drawback, which has been observed in several studies (Boithias et al., 2014; Bieger et al., 2014;  
549 Fohrer et al., 2014; Loukas and Vasiliades, 2014). We observed a similar trend in sub-surface  
550 flow predicted by HSPF. However, in our LSTM-based models, this problem is partially solved.  
551 We can observe large gap between predicted and observed flow duration curve in Figure S12  
552 while this gap is smaller for LSTM-based models (Figure S13, Figure S14). The simple LSTM  
553 model captured peaks in surface runoff more accurately as compared to those predicted by the  
554 HRU-based LSTM model. This trend was also found in the total estimated discharge from each  
555 model. When peaks in surface runoff are underestimated, peaks in total discharge are also  
556 underestimated (Figure 9 and Figure 10), and when peaks in surface runoff are better estimated,  
557 peaks in total discharge are also better estimated (Figure 7 and Figure 8). This means that the  
558 predicted surface runoff mainly contributes to peaks in streamflow while the sub-surface flow  
559 makes up the baseflow portion. This makes our LSTM-based models closer to real observations.

#### 560 **4.4 Challenges and limitations of LSTM models**

561 Calibrating NN for surface flow is extremely challenging. The reason for this is that 96%  
562 of the surface flow data consists of zeros because discernable surface runoff only happens during  
563 rainfall events. This problem is similar to anomaly detection or rare event detection where less

564 than 5–10% of the total data is positively labeled. We observed during HPO iterations that total  
565 surface flow did not change once it became zero upon further calibration of model. It can be  
566 argued that as 96% of surface flow has one unique value, i.e., zero, the network learns to predict  
567 zeros. The matching of the surface flow curve became more challenging because surface flow  
568 does not always coincide with rainfall events. Indeed, during the hot and dry season (generally  
569 from January to April), the soil is dry and evapotranspiration is high. Indeed, the potential  
570 evapotranspiration is higher than rainfall during this period (**Table S2**). For small rainfall events  
571 during this hot and dry season, rainfall is either evapotranspired or infiltrated, however, it is not  
572 transferred to the stream by surface runoff. Precipitation absorbed by the soil may later become  
573 part of sub-surface flow. Calibrating a NN to learn this behavior is the most difficult part, and if  
574 hyper-parameters are not chosen appropriately, the model fails to generalize the surface flow  
575 patterns.

576         Surface and sub-surface flows obtained for each of the 36 HRUs using HRU-based  
577 LSTM model are plotted in Figure S6. By comparing these HRU-specific surface and sub-  
578 surface responses with the HRU-specific input data (**Figure S7 and S8**), we cannot draw a one to  
579 one correspondence between HRU-specific input data and the corresponding output. In certain  
580 cases, an LSTM produces no outflow even when it receives precipitation; thus, all LSTMs in our  
581 HRU-specific model are not necessarily representative of HRU-specific inputs. This can be  
582 because NNs act as black-box models, and the inner workings of these networks are random  
583 ([Karpadne et al., 2017](#)). Thus we cannot draw a simple link between the weights of a NN and the  
584 function being approximated. Another reason for these unpredictable HRU-specific outputs  
585 could be that we used separate NN for each HRU. This means that each of these NNs have  
586 separate weights and biases; thus, if one network gets higher input values of curve number or

587 precipitation, it is completely independent of what the other networks receive as input. Thus,  
588 each network forms its own ‘context’ when it calibrates its weights and biases by looking at the  
589 total output of the whole model.

590 The interest of model interpretability has increased in the field of machine learning  
591 (Samek, W. 2019). Several studies have proposed the ways to incorporate scientific knowledge  
592 into deep learning (Karpatne et al., 2017; Karpatne et al., 2017b; Wang et al., 2020). The  
593 suggested method in our study, the neural network down into sub-models for each HRU, would  
594 be a way to introduce more interpretability into a data-driven models in that this approach can  
595 analyze sub-models in the neural network.

## 596 **5. Conclusions**

597 In this study, we modeled the surface and sub-surface flow using three models: one  
598 lumped model called HSPF and two deep learning models. One deep learning model consisted of  
599 a single LSTM representing the whole catchment, whereas the second model consisted of  
600 LSTMs representing each HRU. All three models predicted total flow, surface and sub-surface  
601 flow separately. The following conclusions were then derived from the results:

- 602 • By replacing the constant values of the area factors in the HSPF model with time series  
603 values, we were able to model land use changes in a catchment.
- 604 • Although HSPF was able to estimate surface and sub-surface flow simultaneously, it  
605 over-estimated surface runoff and under-estimated sub-surface flow. Contrary to this, our  
606 deep learning models were more consistent in predicting surface and sub-surface flow.  
607 Therefore, deep learning models are more suitable when prediction of both surface and  
608 sub-surface flow is required simultaneously.

- 609       • The simple LSTM model, where one LSTM layer is used to represent the whole  
610       catchment, performed best for surface runoff prediction during both calibration and test  
611       period.
- 612       • The HRU-based LSTM model performed better than simple LSTM model for sub-surface  
613       flow prediction during both test and calibration period. It has the best performance for  
614       total streamflow simulation during test period.

615       Understanding the combined impact of climate change and land use changes on the  
616       catchment by modeling surface and sub-surface flows at a very high temporal resolution of 6 min  
617       can help assessing extreme low and extreme high discharge, and improve water resource  
618       management. This would allow more accurate modeling of pollutants (e.g. fecal bacteria) whose  
619       concentrations vary exponentially with time. This study presents a methodology for  
620       incorporating land use changes into hydrological models of surface and sub-surface flow at  
621       catchment scale. This study also demonstrates that deep learning can be an alternative to  
622       physically based or conceptual models by taking in account model complexity at spatial and  
623       temporal scales.

## 624       **5. Acknowledgement**

625       This work was supported by the National Research Foundation of Korea (NRF) grant funded by  
626       the Korea government (MSIT) (NRF-2018K1A3A1A21041779). The authors sincerely thank the  
627       Lao Department of Agricultural Land Management (DALaM) for its support, including granting  
628       the permission for field access, and the M-TROPICS Critical Zone Observatory  
629       (<https://mtropics.obs-mip.fr/>), which belongs to the French Research Infrastructure OZCAR  
630       (<http://www.ozcar-ri.org/>), for data access.

631 **6. References**

- 632 Abadi, M., Barham, P., Chen, J., Chen, Z., Davis, A., Dean, J., ... & Kudlur, M. 2016. Tensorflow: A system  
633 for large-scale machine learning. In 12th {USENIX} Symposium on Operating Systems Design and  
634 Implementation ({OSDI} 16) 265-283.
- 635 Andrew, G., & Gao, J. 2007. Scalable training of L 1-regularized log-linear models. In Proceedings of the  
636 24th international conference on Machine learning, 33-40.  
637 <https://doi.org/10.1145/1273496.1273501>
- 638 Arnold, J.G., Fohrer, N., 2005. SWAT2000: current capabilities and research opportunities in applied  
639 watershed modelling. *Hydrological Processes: An International Journal*, 19(3), 563-572.  
640 <https://doi.org/10.1002/hyp.5611>
- 641 Adie, H. T. R., & Pradana, I. A. 2018. Parallel computing accelerated image inpainting using GPU CUDA,  
642 Theano, and Tensorflow. In *2018 10th International Conference on Information Technology and  
643 Electrical Engineering (ICITEE)*, 621-625. IEEE. <https://doi.org/10.1109/ICITEED.2018.8534858>
- 644 Baek, S.-S. et al., 2017. Developing a hydrological simulation tool to design bioretention in a watershed.  
645 *Environmental Modelling & Software*. <https://doi.org/10.1016/j.envsoft.2017.11.006>
- 646 Benítez, J.M., Castro, J.L., Requena, I., 1997. Are artificial neural networks black boxes? *IEEE Transactions  
647 on neural networks*, 8(5), 1156-1164. <https://doi.org/10.1109/72.623216>
- 648 Bennett, J.C., Robertson, D.E., Ward, P.G., Hapuarachchi, H.P., Wang, Q., 2016. Calibrating hourly  
649 rainfall-runoff models with daily forcings for streamflow forecasting applications in meso-scale  
650 catchments. *Environmental Modelling & Software*, 76, 20-36.  
651 <https://doi.org/10.1016/j.envsoft.2015.11.006>
- 652 Bergstra, J. S., Bardenet, R., Bengio, Y., & Kégl, B. 2011. Algorithms for hyper-parameter optimization. In  
653 *Advances in neural information processing systems*, 2546-2554.
- 654 Bergstra, J., Komer, B., Eliasmith, C., Yamins, D., & Cox, D. D. 2015. Hyperopt: a python library for model  
655 selection and hyperparameter optimization. *Computational Science & Discovery*, 8(1), 014008.
- 656 Besaw, L.E., Rizzo, D.M., Bierman, P.R., Hackett, W.R., 2010. Advances in ungauged streamflow  
657 prediction using artificial neural networks. *Journal of Hydrology*, 386(1-4), 27-37.  
658 <https://doi.org/10.1016/j.jhydrol.2010.02.037>
- 659 Bicknell, B.R. et al., 2001. Hydrological simulation program-Fortran: HSPF version 12 user's manual.  
660 AQUA TERRA Consultants, Mountain View, California, 845.
- 661 Bieger, K., Hörmann, G., Fohrer, N., 2014. Simulation of streamflow and sediment with the soil and  
662 water assessment tool in a data scarce catchment in the three Gorges region, China. *Journal of  
663 environmental quality*, 43(1), 37-45. <http://doi.org/10.2134/jeq2011.0383>
- 664 Boithias, L. et al., 2017. Simulating flash floods at hourly time-step using the SWAT model. *Water*, 9(12),  
665 929. <http://doi.org/10.3390/w9120929>
- 666 Boithias, L., Srinivasan, R., Sauvage, S., Macary, F., Sánchez-Pérez, J.M., 2014. Daily nitrate losses:  
667 implication on long-term river quality in an intensive agricultural catchment of southwestern  
668 France. *Journal of environmental quality*, 43(1), 46-54. <http://doi.org/10.2134/jeq2011.0367>
- 669 Bressiani, D.d.A. et al., 2015. Review of soil and water assessment tool (SWAT) applications in Brazil:  
670 Challenges and prospects. *International Journal of Agricultural and Biological Engineering*, 8(3),  
671 9-35. <http://doi.org/10.3965/j.ijabe.20150803.1765>
- 672 Burns, D.A., Kendall, C., 2002. Analysis of  $\delta^{15}\text{N}$  and  $\delta^{18}\text{O}$  to differentiate  $\text{NO}_3^-$  sources in runoff at two  
673 watersheds in the Catskill Mountains of New York. *Water Resources Research*, 38(5), 9-1-9-11.  
674 <https://doi.org/10.1029/2001WR000292>

675 Campos, L.C.D. et al., 2019. Short-Term Streamflow Forecasting for Paraíba do Sul River Using Deep  
676 Learning, EPIA Conference on Artificial Intelligence. Springer. 507-518.

677 Chaplot, V.A., Rumpel, C., Valentin, C., 2005. Water erosion impact on soil and carbon redistributions  
678 within uplands of Mekong River. *Global biogeochemical cycles*, 19(4).  
679 <https://doi.org/10.1029/2005GB002493>

680 Chen, Y., & Li, Y. 2018. Computational intelligence assisted design: in industrial revolution 4.0. CRC Press.

681 Cho, K. et al., 2014. Learning phrase representations using RNN encoder-decoder for statistical machine  
682 translation. *arXiv preprint arXiv:1406.1078*.

683 Debele, B., Srinivasan, R., Parlange, J.-Y., 2009. Hourly analyses of hydrological and water quality  
684 simulations using the ESWAT model. *Water resources management*, 23(2), 303-324.

685 Dewancker, I., McCourt, M., & Clark, S. 2015. Bayesian optimization primer.

686 Diaz-Ramirez, J., Johnson, B., McAnally, W., Martin, J., Alarcon, V., 2013. Estimation and Propagation of  
687 Parameter Uncertainty in Lumped Hydrological Models: A Case Study of HSPF Model Applied to  
688 Luxapallila Creek Watershed in Southeast USA. *J Hydrogeol Hydrol Eng* 2: 1. of, 9, 2.  
689 <http://dx.doi.org/10.4172/2325-9647.1000105>

690 Frazier, P. I. 2018. A tutorial on bayesian optimization. *arXiv preprint arXiv:1807.02811*.

691 Ficchi, A., Perrin, C., Andréassian, V., 2016. Impact of temporal resolution of inputs on hydrological  
692 model performance: An analysis based on 2400 flood events. *Journal of Hydrology*, 538, 454-470.  
693 <https://doi.org/10.1016/j.jhydrol.2016.04.016>

694 Fohrer, N., Dietrich, A., Kolychalov, O., Ulrich, U., 2014. Assessment of the environmental fate of the  
695 herbicides flufenacet and metazachlor with the SWAT model. *Journal of environmental quality*,  
696 43(1), 75-85. <http://doi.org/10.2134/jeq2011.0382>

697 Fukushima, K., 1980. Neocognitron: A self-organizing neural network model for a mechanism of pattern  
698 recognition unaffected by shift in position. *Biological cybernetics*, 36(4), 193-202.  
699 <https://doi.org/10.1007/BF00344251>

700 Gaillardet, J. et al., 2018. OZCAR: the French network of critical zone observatories. *Vadose Zone Journal*,  
701 17(1).

702 Gassman, P.W., Reyes, M.R., Green, C.H., Arnold, J.G., 2007. The soil and water assessment tool:  
703 historical development, applications, and future research directions. *Transactions of the ASABE*,  
704 50(4), 1211-1250. <https://doi.org/10.13031/2013.23637>

705 Goodfellow, I., Bengio, Y., Courville, A., 2016. Deep learning. MIT press.

706 Grams, J. S., Gallus Jr, W. A., Koch, S. E., Wharton, L. S., Loughe, A., & Ebert, E. E. 2006. The use of a  
707 modified Ebert–McBride technique to evaluate mesoscale model QPF as a function of  
708 convective system morphology during IHOP 2002. *Weather and forecasting*, 21(3), 288-306.  
709 <https://doi.org/10.1175/WAF918.1>

710 Granata, F., Gargano, R., de Marinis, G., 2016. Support vector regression for rainfall-runoff modeling in  
711 urban drainage: A comparison with the EPA’s storm water management model. *Water*, 8(3), 69.

712 Greff, K., Srivastava, R.K., Koutník, J., Steunebrink, B.R., Schmidhuber, J., 2016. LSTM: A search space  
713 odyssey. *IEEE transactions on neural networks and learning systems*, 28(10), 2222-2232.  
714 <http://doi.org/10.1109/TNNLS.2016.2582924>

715 Gupta, H.V., Kling, H., Yilmaz, K.K., Martinez, G.F., 2009. Decomposition of the mean squared error and  
716 NSE performance criteria: Implications for improving hydrological modelling. *Journal of  
717 hydrology*, 377(1-2), 80-91. <https://doi.org/10.1016/j.jhydrol.2009.08.003>

718 Guse, B., Reusser, D.E., Fohrer, N., 2014. How to improve the representation of hydrological processes in  
719 SWAT for a lowland catchment–temporal analysis of parameter sensitivity and model  
720 performance. *Hydrological processes*, 28(4), 2651-2670. <https://doi.org/10.1002/hyp.9777>



721 Hoang, L. et al., 2014. Comparison and evaluation of model structures for the simulation of pollution  
722 fluxes in a tile-drained river basin. *Journal of environmental quality*, 43(1), 86-99.  
723 <https://doi.org/10.2134/jeq2011.0398>

724 Hochreiter, S., 1998. The vanishing gradient problem during learning recurrent neural nets and problem  
725 solutions. *International Journal of Uncertainty, Fuzziness and Knowledge-Based Systems*, 6(02),  
726 107-116.

727 Hochreiter, S., Schmidhuber, J., 1997. Long short-term memory. *Neural computation*, 9(8), 1735-1780.

728 Huang, P., Li, Z., Yao, C., Li, Q., Yan, M., 2016. Spatial combination modeling framework of saturation-  
729 excess and infiltration-excess runoff for semihumid watersheds. *Advances in Meteorology*, 2016.  
730 <http://dx.doi.org/10.1155/2016/5173984>

731 Huang, Y., Bárdossy, A., Zhang, K., 2019. Sensitivity of hydrological models to temporal and spatial  
732 resolutions of rainfall data. *Hydrology and Earth System Sciences*, 23(6), 2647-2663.  
733 <https://doi.org/10.5194/hess-23-2647-2019>

734 Hutter, F., Lücke, J., Schmidt-Thieme, L., 2015. Beyond manual tuning of hyperparameters. *KI-Künstliche*  
735 *Intelligenz*, 29(4), 329-337. <https://doi.org/10.1007/s13218-015-0381-0>

736 Ilunga, M., Stephenson, D., 2005. Infilling streamflow data using feed-forward back-propagation (BP)  
737 artificial neural networks: application of standard BP and Pseudo Mac Laurin power series BP  
738 techniques. *Water SA*, 31(2), 171-176. <http://dx.doi.org/10.4314/wsa.v31i2.5199>

739 Jeong, J. et al., 2010. Development and integration of sub-hourly rainfall–runoff modeling capability  
740 within a watershed model. *Water Resources Management*, 24(15), 4505-4527.  
741 <http://doi.org/10.1007/s11269-010-9670-4>

742 Jodar-Abellan, A., Valdes-Abellan, J., Pla, C., Gomariz-Castillo, F., 2019. Impact of land use changes on  
743 flash flood prediction using a sub-daily SWAT model in five Mediterranean ungauged  
744 watersheds (SE Spain). *Science of the Total Environment*, 657, 1578-1591.  
745 <https://doi.org/10.1016/j.scitotenv.2018.12.034>

746 Johanson, R.C., Davis, H.H., 1980. Users manual for hydrological simulation program-Fortran (HSPF), 80.  
747 Environmental Research Laboratory, Office of Research and Development, US ...

748 Jones, D. R., Schonlau, M., & Welch, W. J. 1998. Efficient global optimization of expensive black-box  
749 functions. *Journal of Global optimization*, 13(4), 455-492.  
750 <https://doi.org/10.1023/A:1008306431147>

751 Jones, E., Oliphant, T., Peterson, P., 2001. SciPy: Open source scientific tools for Python.

752 Karpatne, A. et al., 2017. Theory-guided data science: A new paradigm for scientific discovery from data.  
753 *IEEE Transactions on Knowledge and Data Engineering*, 29(10), 2318-2331.  
754 <https://doi.org/10.1109/TKDE.2017.2720168>

755 Karpatne, A., Watkins, W., Read, J., & Kumar, V. 2017b. Physics-guided neural networks (pgnn): An  
756 application in lake temperature modeling. *arXiv preprint arXiv:1710.11431*.

757 Kim, M., Boithias, L., Cho, K.H., Sengtaheuanghoung, O., Ribolzi, O., 2018. Modeling the impact of land  
758 use change on basin-scale transfer of fecal indicator bacteria: SWAT model performance. *Journal*  
759 *of environmental quality*, 47(5), 1115-1122. <http://doi.org/10.2134/jeq2017.11.0456>

760 Kinerson, R.S., Kittle, J.L., Duda, P.B., 2009. BASINS: Better assessment science integrating point and  
761 nonpoint sources, *Decision Support Systems for Risk-Based Management of Contaminated Sites*.  
762 Springer, pp. 1-24. <http://doi.org/10.1007/978-0-387-09722-0>

763 Kratzert, F., Klotz, D., Brenner, C., Schulz, K., Herrnegger, M., 2018. Rainfall–runoff modelling using long  
764 short-term memory (LSTM) networks. *Hydrology and Earth System Sciences*, 22(11), 6005-6022.  
765 <https://doi.org/10.5194/hess-22-6005-2018>

766 Kratzert, F., Klotz, D., Shalev, G., Klambauer, G., Hochreiter, S., & Nearing, G. 2019. Towards learning  
767 universal, regional, and local hydrological behaviors via machine learning applied to large-  
768 sample datasets. *arXiv preprint arXiv:1907.08456*. <https://doi.org/10.5194/hess-23-5089-2019>

769 Kratzert, F., Herrnegger, M., Klotz, D., Hochreiter, S., & Klambauer, G. 2019b. NeuralHydrology–  
770 Interpreting LSTMs in Hydrology. In *Explainable AI: Interpreting, Explaining and Visualizing Deep*  
771 *Learning* (pp. 347-362). Springer, Cham. [https://doi.org/10.1007/978-3-030-28954-6\\_19](https://doi.org/10.1007/978-3-030-28954-6_19)

772 Kumar, G.M., Head, T., 2017. Scikit-optimize. Tim Head and contributors

773 Lakhmiri, D., Digabel, S. L., & Tribes, C. 2019. HyperNOMAD: Hyperparameter optimization of deep  
774 neural networks using mesh adaptive direct search. *arXiv preprint arXiv:1907.01698*.

775 Le, X.-H., Ho, H.V., Lee, G., Jung, S., 2019. Application of Long Short-Term Memory (LSTM) Neural  
776 Network for Flood Forecasting. *Water*, 11(7), 1387.

777 Li, W., Kiaghadi, A., & Dawson, C. N. 2020. High Temporal Resolution Rainfall Runoff Modelling Using  
778 Long-Short-Term-Memory (LSTM) Networks. *arXiv preprint arXiv:2002.02568*.  
779 <https://doi.org/10.1007/s00521-020-05010-6>

780 lin Hsu, K., Gupta, H.V., Sorooshian, S., 1997. Application of a recurrent neural network to rainfall-runoff  
781 modeling, *Proceedings of the 1997 24th Annual Water Resources Planning and Management*  
782 *Conference*. ASCE. 68-73.

783 Loukas, A., Vassiliades, L., 2014. Streamflow simulation methods for ungauged and poorly gauged  
784 watersheds. *Natural Hazards and Earth System Sciences*, 14(7), 1641-1661.  
785 <https://doi.org/10.4296/cwrj2804633>

786 Makridakis, S., Spiliotis, E., Assimakopoulos, V., 2018. Statistical and Machine Learning forecasting  
787 methods: Concerns and ways forward. *PloS one*, 13(3), e0194889.  
788 <https://doi.org/10.1371/journal.pone.0194889>

789 Mockus, J., Tiesis, V., & Zilinskas, A. 1978. The application of Bayesian methods for seeking the  
790 extremum. *Towards global optimization*, 2(117-129), 2.

791 Moriasi, D.N., Gitau, M.W., Pai, N., Daggupati, P., 2015. Hydrologic and water quality models:  
792 Performance measures and evaluation criteria. *Transactions of the ASABE*, 58(6), 1763-1785.  
793 <https://doi.org/10.13031/trans.58.10715>

794 Mosavi, A., Ozturk, P., Chau, K.-w., 2018. Flood prediction using machine learning models: Literature  
795 review. *Water*, 10(11), 1536.

796 Munna, G. M., Kibriya, N. A., Nury, A. H., Islam, S., & Rahman, H. 2015. Spatial distribution analysis and  
797 mapping of groundwater quality parameters for the Sylhet City Corporation (SCC) area using GIS.  
798 *Hydrology*, 3(1), 1-10. <https://doi.org/10.11648/j.hyd.20150301.11>

799 Nash, S.G., 1984. Newton-type minimization via the Lanczos method. *SIAM Journal on Numerical*  
800 *Analysis*, 21(4), 770-788.

801 Ogwueleka, T.C., Ogwueleka, F.N., 2009. Feed-forward neural networks for precipitation and river level  
802 prediction. *Adv. Natl. Appl. Sci*, 3, 350-356.

803 Ouellet-Proulx, S., St-Hilaire, A., Boucher, M.A., 2019. Implication of evaporative loss estimation  
804 methods in discharge and water temperature modelling in cool temperate climates.  
805 *Hydrological Processes*. <https://doi.org/10.1002/hyp.13534>

806 Pang, S., Wang, X., Ma, W., 2018. Research of Parameter Uncertainty for the HSPF Model Under  
807 Different Temporal Scales. *Huan jing ke xue= Huanjing kexue*, 39(5), 2030-2038.  
808 <http://doi.org/10.13227/j.hjxk.201710070>

809 Papalexiou, S.M., Montanari, A., 2019. Global and Regional Increase of Precipitation Extremes under  
810 Global Warming. *Water Resources Research*.

811 Park, S. et al., 2019. Deep neural networks for modeling fouling growth and flux decline during NF/RO  
812 membrane filtration. *Journal of Membrane Science*.

813 Pascual, X. et al., 2013. Data-driven models of steady state and transient operations of spiral-wound RO  
814 plant. *Desalination*, 316, 154-161.

815 Patin, J. et al., 2018. Effect of land use on interrill erosion in a montane catchment of Northern Laos: An  
816 analysis based on a pluri-annual runoff and soil loss database. *Journal of hydrology*, 563, 480-  
817 494.

818 Prudhomme, C., Williamson, J., 2013. Derivation of RCM-driven potential evapotranspiration for  
819 hydrological climate change impact analysis in Great Britain: a comparison of methods and  
820 associated uncertainty in future projections. *Hydrology and Earth System Sciences*, 17(4), 1365-  
821 1377.

822 Reynolds, J., Halldin, S., Xu, C.-Y., Seibert, J., Kauffeldt, A., 2017. Sub-daily runoff predictions using  
823 parameters calibrated on the basis of data with a daily temporal resolution. *Journal of hydrology*,  
824 550, 399-411.

825 Ribolzi, O. et al., 2017. From shifting cultivation to teak plantation: effect on overland flow and sediment  
826 yield in a montane tropical catchment. *Scientific reports*, 7(1), 3987.  
827 <https://doi.org/10.1038/s41598-017-04385-2>

828 Ribolzi, O. et al., 2016. Use of fallout radionuclides (<sup>7</sup>Be, <sup>210</sup>Pb) to estimate resuspension of  
829 *Escherichia coli* from streambed sediments during floods in a tropical montane catchment.  
830 *Environmental Science and Pollution Research*, 23(4), 3427-3435.

831 Ribolzi, O. et al., 2018. Interacting land use and soil surface dynamics control groundwater outflow in a  
832 montane catchment of the lower Mekong basin. *Agriculture, ecosystems & environment*, 268,  
833 90-102. <https://doi.org/10.1016/j.agee.2018.09.005>

834 Rossman, L.A., 2010. Storm water management model user's manual, version 5.0. National Risk  
835 Management Research Laboratory, Office of Research and ....

836 Roxy, M.K. et al., 2017. A threefold rise in widespread extreme rain events over central India. *Nature*  
837 *communications*, 8(1), 708.

838 Rumelhart, D.E., Hinton, G.E., Williams, R.J., 1988. Learning representations by back-propagating errors.  
839 *Cognitive modeling*, 5(3), 1. <https://doi.org/10.1038/323533a0>

840 Samek, W. (2019). *Explainable AI: interpreting, explaining and visualizing deep learning* (Vol. 11700).  
841 Springer Nature.

842 Shahriari, B., Swersky, K., Wang, Z., Adams, R. P., & De Freitas, N. 2015. Taking the human out of the  
843 loop: A review of Bayesian optimization. *Proceedings of the IEEE*, 104(1), 148-175.

844 Shen, C., 2018. A transdisciplinary review of deep learning research and its relevance for water  
845 resources scientists. *Water Resources Research*, 54(11), 8558-8593.  
846 <https://doi.org/10.1029/2018WR022643>

847 Singh, V.P., 1988. *Hydrologic systems: Rainfall-runoff modeling*.

848 Snoek, J., Rippel, O., Swersky, K., Kiros, R., Satish, N., Sundaram, N., ... & Adams, R. 2015. Scalable  
849 bayesian optimization using deep neural networks. In *International conference on machine*  
850 *learning*. 2171-2180.

851 Spruill, C.A., Workman, S.R., Taraba, J.L., 2000. Simulation of daily and monthly stream discharge from  
852 small watersheds using the SWAT model. *Transactions of the ASAE*, 43(6), 1431.  
853 <https://doi.org/10.13031/2013.3041>

854 Stern, M., Flint, L., Minear, J., Flint, A., Wright, S., 2016. Characterizing changes in streamflow and  
855 sediment supply in the Sacramento River Basin, California, using hydrological simulation  
856 program—FORTRAN (HSPF). *Water*, 8(10), 432. <https://doi.org/10.3390/w8100432>

857 Talei, A., Chua, L.H., 2012. Influence of lag time on event-based rainfall–runoff modeling using the data  
858 driven approach. *Journal of Hydrology*, 438, 223-233.

- 859 Wang, N., Zhang, D., Chang, H., & Li, H. 2020. Deep learning of subsurface flow via theory-guided neural  
860 network. *Journal of Hydrology*, 584, 124700. <https://doi.org/10.1016/j.jhydrol.2020.124700>
- 861 Wang, Y., He, B., Takase, K., 2009. Effects of temporal resolution on hydrological model parameters and  
862 its impact on prediction of river discharge/Effets de la résolution temporelle sur les paramètres  
863 d'un modèle hydrologique et impact sur la prévision de l'écoulement en rivière. *Hydrological  
864 sciences journal*, 54(5), 886-898.
- 865 Xie, H., Lian, Y., 2013. Uncertainty-based evaluation and comparison of SWAT and HSPF applications to  
866 the Illinois River Basin. *Journal of Hydrology*, 481, 119-131.  
867 <https://doi.org/10.1016/j.jhydrol.2012.12.027>
- 868 Yan, L., Feng, J., Hang, T., 2019. Small Watershed Stream-Flow Forecasting Based on LSTM, *International  
869 Conference on Ubiquitous Information Management and Communication*. Springer. 1006-1014.
- 870 Yaseen, Z.M., El-Shafie, A., Jaafar, O., Afan, H.A., Sayl, K.N., 2015. Artificial intelligence based models for  
871 stream-flow forecasting: 2000–2015. *Journal of Hydrology*, 530, 829-844.  
872 <https://doi.org/10.1016/j.jhydrol.2015.10.038>
- 873 Yeh, H.-F., 2017. Comparison of evapotranspiration methods under limited data. In: Bucur, D. (Ed.),  
874 *Current perspective to predict actual evapotranspiration*.  
875 <https://doi.org/10.5772/intechopen.68495>
- 876 Zhang, J., Zhu, Y., Zhang, X., Ye, M., Yang, J., 2018. Developing a Long Short-Term Memory (LSTM) based  
877 model for predicting water table depth in agricultural areas. *Journal of hydrology*, 561, 918-929.  
878 <https://doi.org/10.1016/j.jhydrol.2018.04.065>
- 879

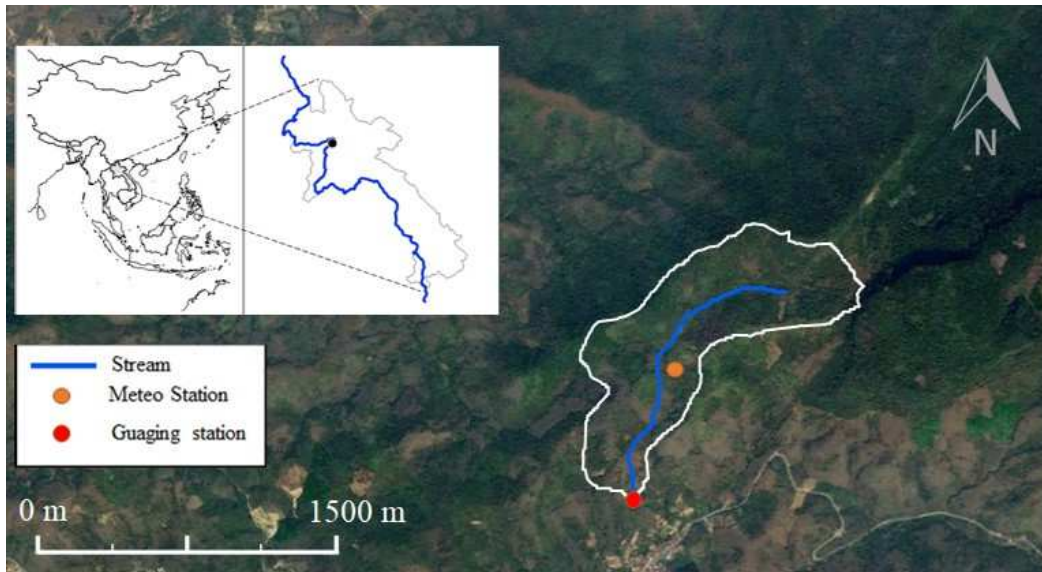


**Figure 1.** Location of the Houay Pano catchment in northern Lao P.D.R. and the observation stations. Topographic map is taken from Google Earth ( $19^{\circ}51'29.49''$  N,  $102^{\circ}10'21.51''$  E) (Google, 2014).

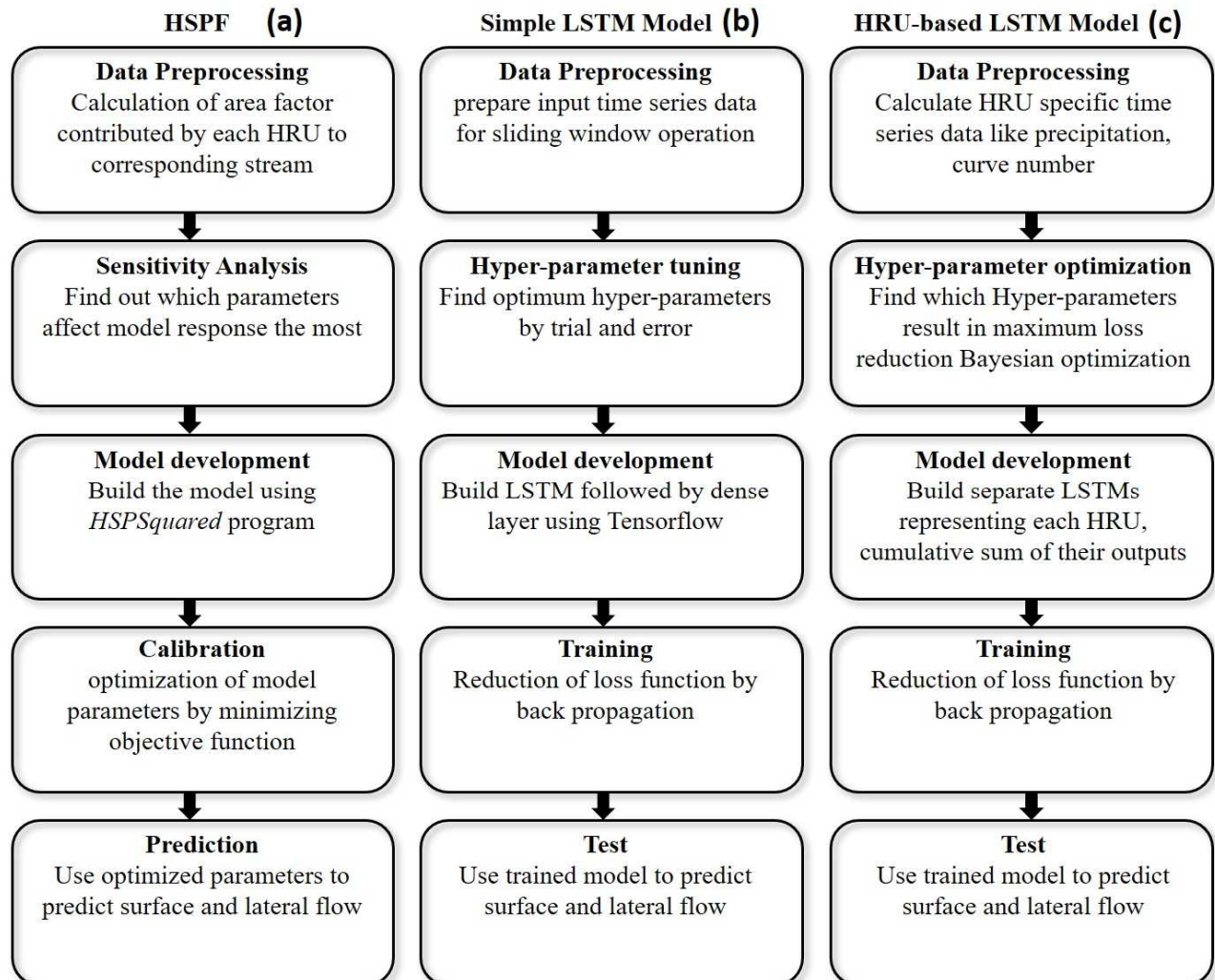


**Figure 2.** Framework for developing (a) HSPF, (b) Simple LSTM Model, and (c) HRU-based LSTM Model. The simple LSTM model consists of one Long Short-Term Memory (LSTM) layer representing the whole catchment, while the HRU-based LSTM model consists of separate LSTMs for each hydrological response unit (HRU). LSTMs are a special kind of neural network specialized for learning patterns in time dependent data. An HRU in the HRU-based model is defined as ‘a distinct land use in a distinct sub-basin’. The output from each of these LSTMs is added in a cumulative manner.

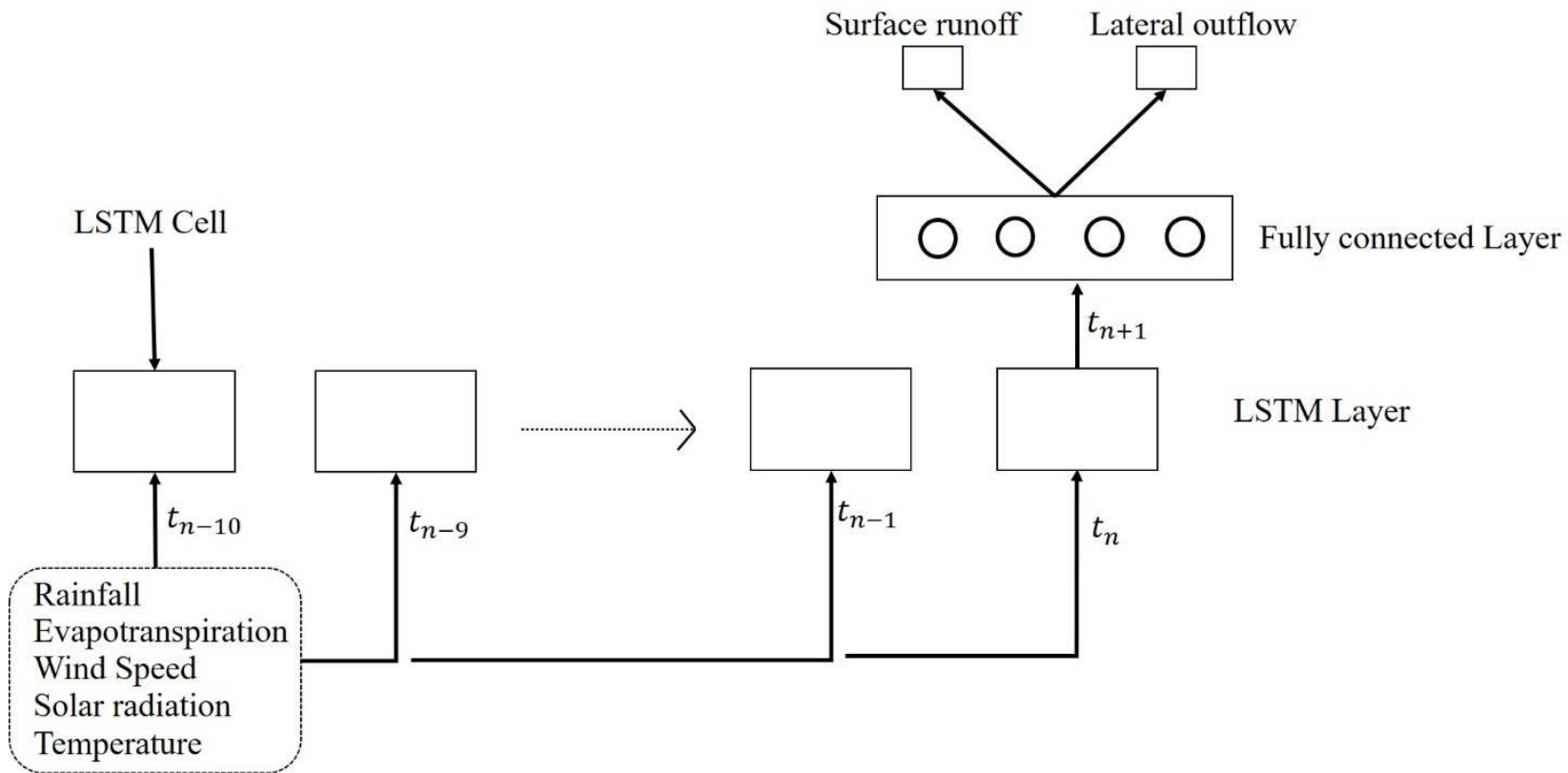


**Figure 3.** Structure of a simple LSTM consisting of an LSTM layer followed by a fully connected layer which generates two outputs. The two outputs are supposed to be representative of surface and sub-surface flow. The LSTM layer consists of LSTM cells, each of which take input at a particular time-step. The diagram represents the working of an NN at time-step ' $t_n$ ' to produce output at  $t_{n+1}$  using a window size of 10.

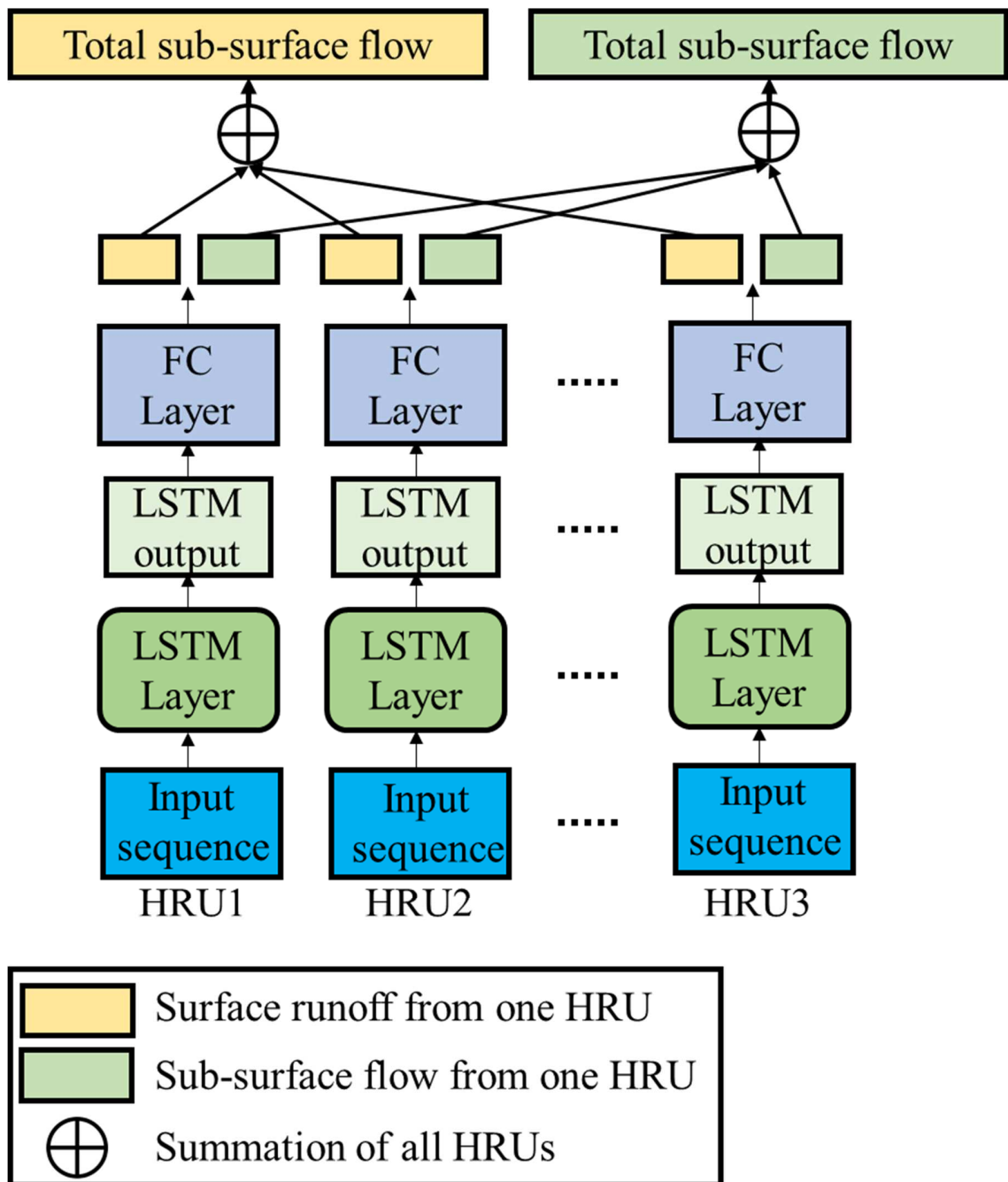


**Figure 4.** Structure of HRU-based LSTM model consisting of 36 parallel layers. Each layer represents one HRU in the catchment. Every LSTM is followed by a dense layer which produces two outputs. These two outputs represent surface and sub-surface flow from one HRU. Finally, surface and sub-surface flow are summed together to get total surface runoff and sub-surface flow.



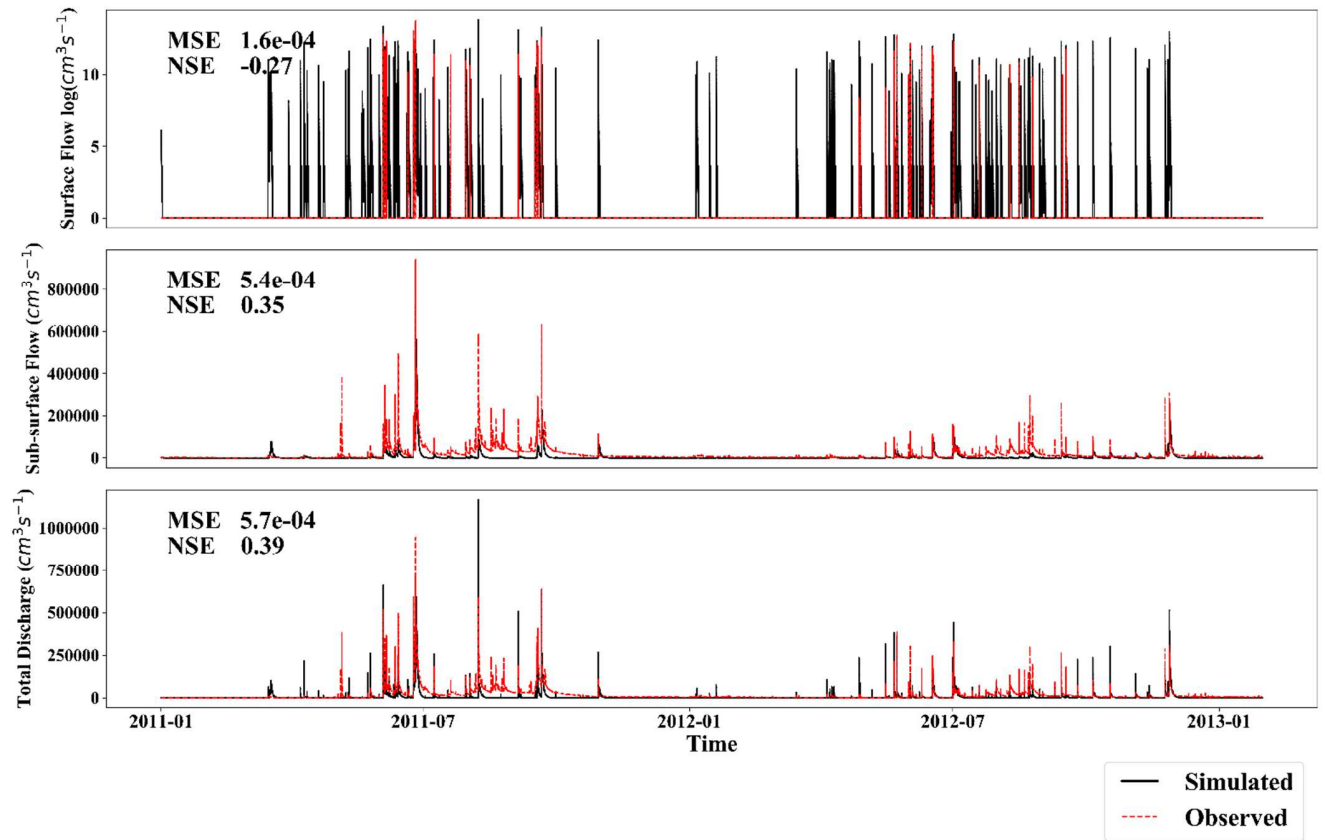


**Figure 5.** Calibration of surface runoff ( $\text{m}^3 \text{s}^{-1}$ ), sub-surface flow ( $\text{m}^3 \text{s}^{-1}$ ), and total discharge ( $\text{m}^3 \text{s}^{-1}$ ) using HSPF model.

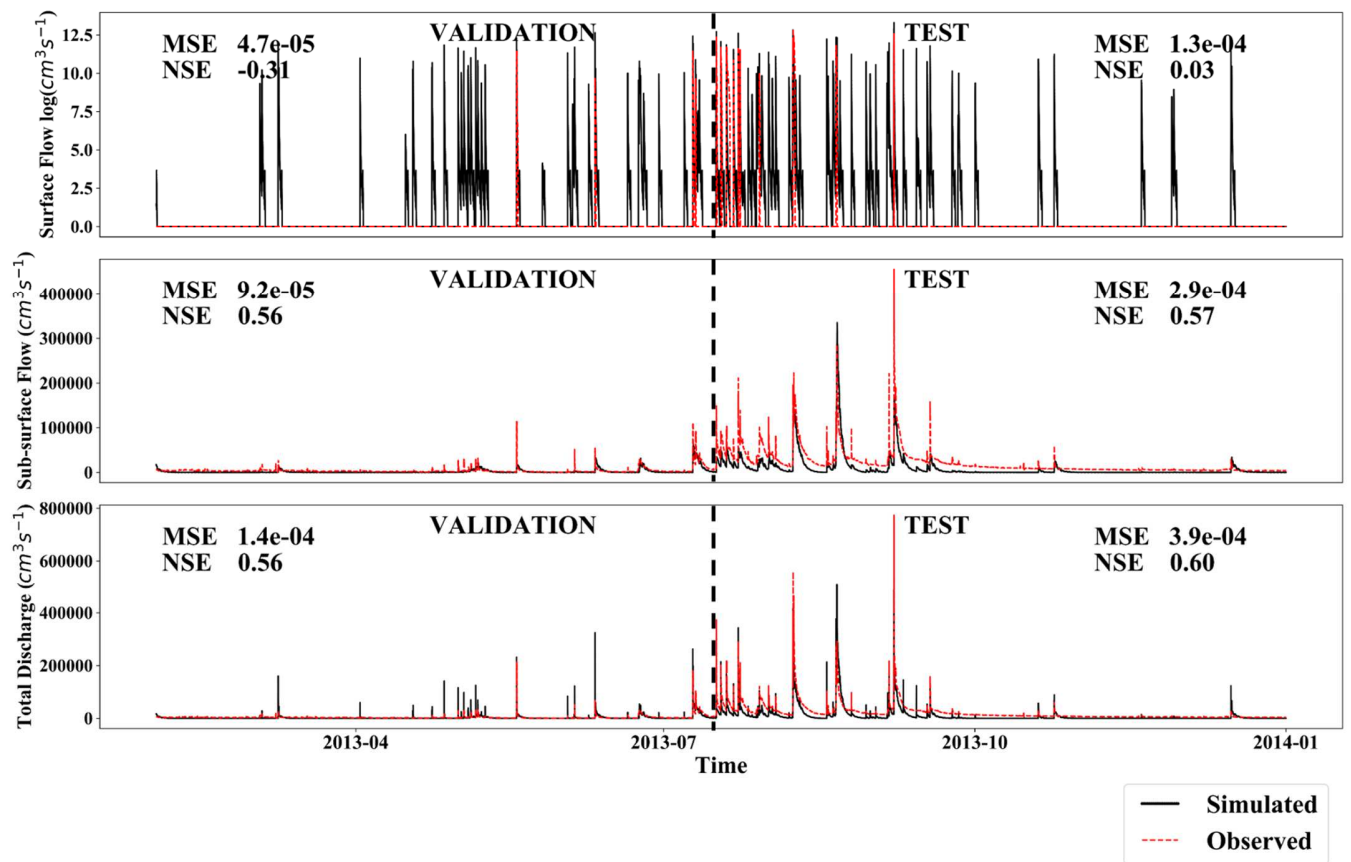


**Figure 6.** Prediction of surface runoff ( $\text{m}^3\text{s}^{-1}$ ), sub-surface flow ( $\text{m}^3\text{s}^{-1}$ ), and total discharge ( $\text{m}^3\text{s}^{-1}$ ) using calibrated HSPF model.

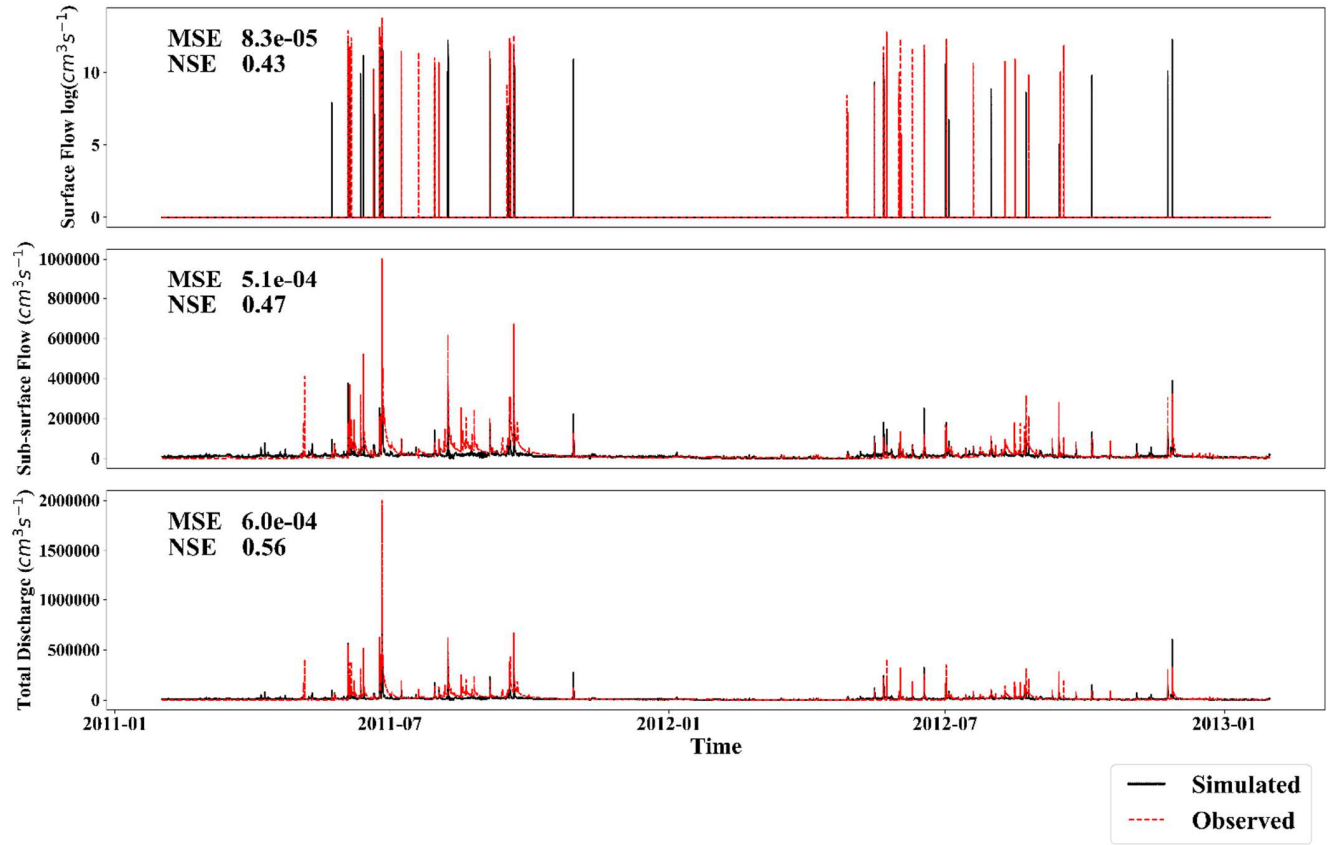


**Figure 7** Calibration of surface runoff ( $\text{m}^3\text{s}^{-1}$ ), sub-surface flow ( $\text{m}^3\text{s}^{-1}$ ), and total discharge ( $\text{m}^3\text{s}^{-1}$ ) using simple LSTM model.

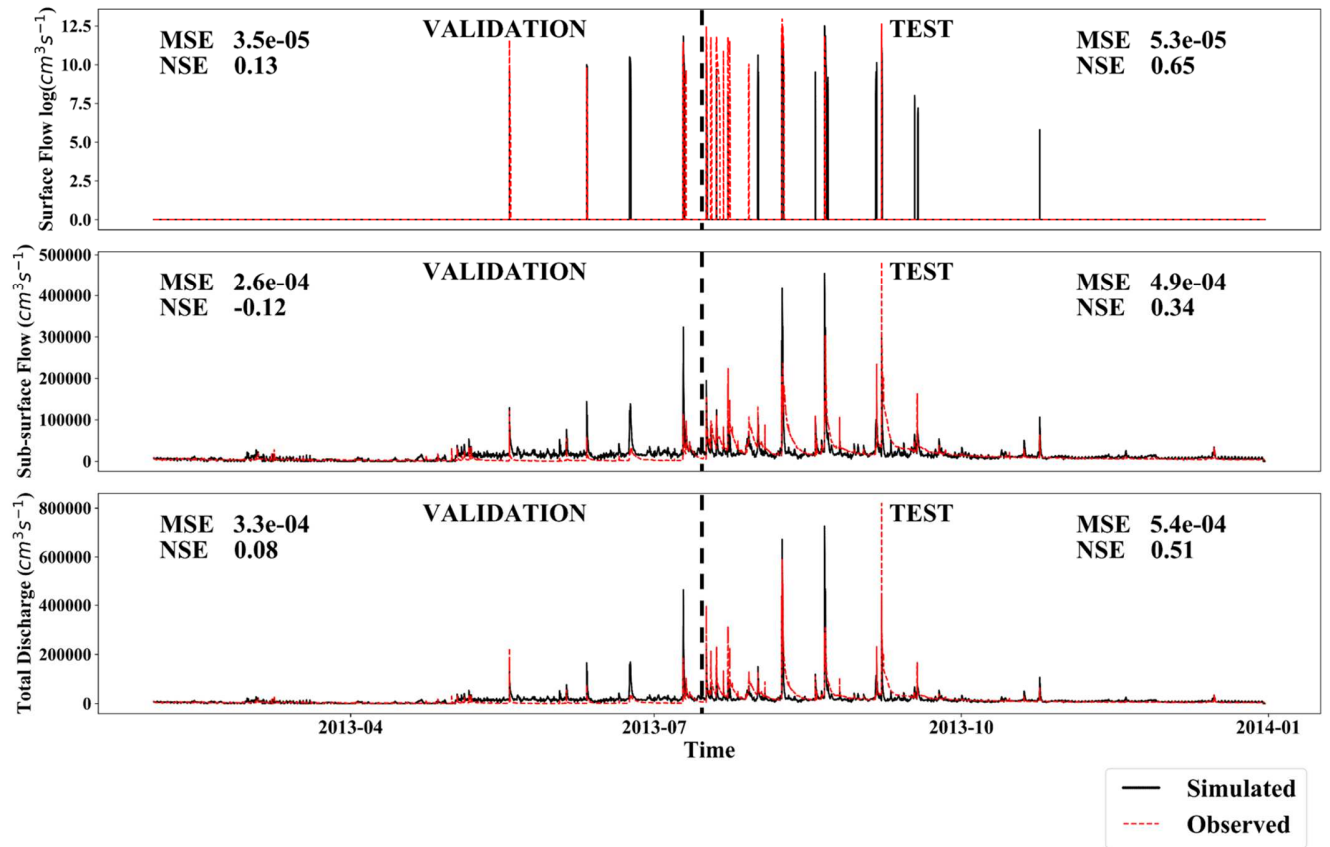


**Figure 8** Prediction surface runoff ( $\text{m}^3 \text{s}^{-1}$ ), sub-surface flow ( $\text{m}^3 \text{s}^{-1}$ ), and total discharge ( $\text{m}^3 \text{s}^{-1}$ ) using calibrated simple LSTM model.

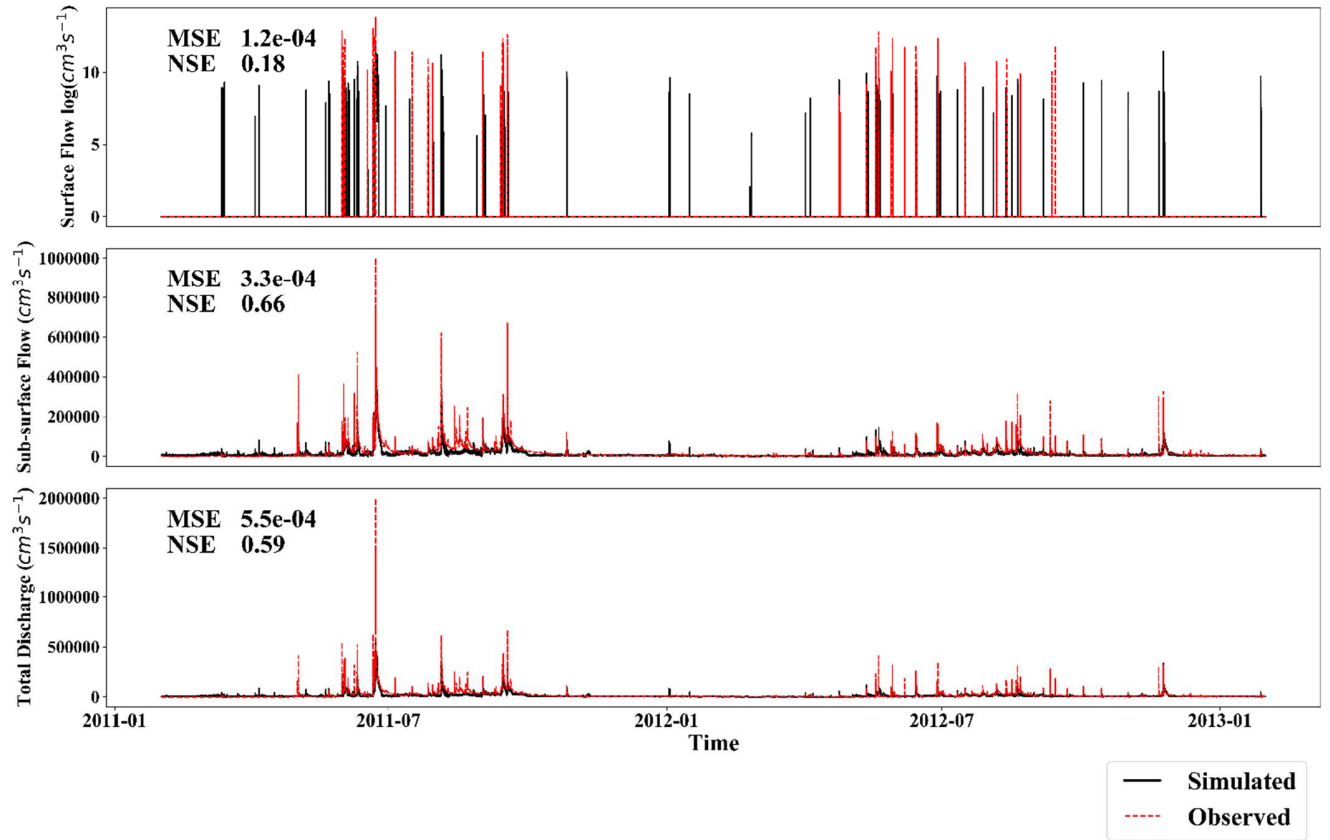


**Figure 9** Calibration of surface runoff ( $\text{m}^3 \text{s}^{-1}$ ), sub-surface flow ( $\text{m}^3 \text{s}^{-1}$ ), and total discharge ( $\text{m}^3 \text{s}^{-1}$ ) using HRU-based LSTM model.

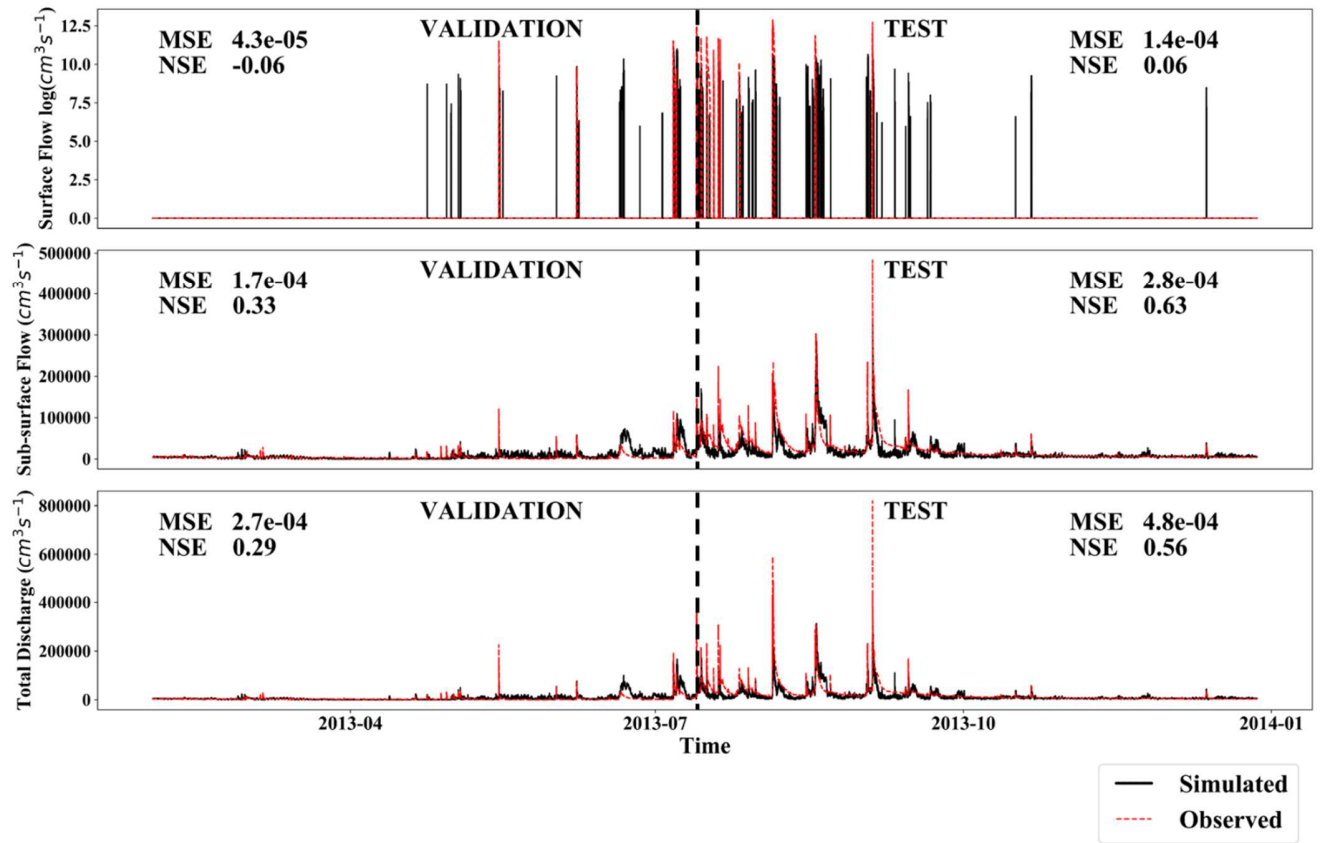


**Figure 10** Prediction of surface runoff ( $\text{m}^3\text{s}^{-1}$ ), sub-surface flow ( $\text{m}^3\text{s}^{-1}$ ), and total discharge ( $\text{m}^3\text{s}^{-1}$ ) using calibrated HRU-based LSTM model.

**Table 1** Hyper-parameters used for building simple and HRU-based LSTM models.

<b>Parameter</b>	<b>Value for simple model</b>	<b>Values for HRU-based model</b>
Activation function	Rectified Linear Unit	Rectified Linear Unit
Batch size	64	64
Learning rate	1e-5	1e-5
Sequence length	13 h	80 h
Hidden units	128	128
Input data	Precipitation moving average, air temperature, precipitation, wind speed, solar radiation	Precipitation moving average, air temperature, precipitation, wind speed, solar radiation, potential evapotranspiration
HRU specific data	None	Rainfall, distance to outlet, curve number
Calibration epochs	214	66

**Table 2** Results of sensitivity analysis of parameters for sub-surface flow and total discharge.

Sub-surface Flow				Total Discharge			
Parameters	Land use	Sensitivity Rank	Calibrated values	Parameters	Land use	Sensitivity Rank	Calibrated values
AGWETP	Fallow	1	0.066	UZSN	Forest	1	2.0
AGWETP	Teak	2	0.0	UZSN	Fallow	2	0.05
AGWETP	Annual crops	3	0.2	INTFW	Forest	3	10.0
AGWETP	Forest	4	0.133	INTFW	Fallow	4	10.0
INFILT	Fallow	5	0.5	UZSN	Teak	5	1.35
INFILT	Forest	6	0.336	INFILT	Forest	6	0.336
INFILT	Annual crops	7	0.5	INFILT	Fallow	7	0.5
INFILT	Teak	8	0.336	INTFW	Teak	8	4.0
BASETP	Forest	9	0.066	UZSN	Annual crops	9	2.0
BASETP	Annual crops	10	0.0	INFILT	Teak	10	0.336
DEEPFR	Fallow	11	0.16	INTFW	Annual crops	11	7.0
DEEPFR	Teak	12	0.0	INFILT	Annual crops	12	0.5



**Table 3.** Performance matrix of HSPF, simple NN, and HRU-based LSTM model. Bold numbers represent values that fall under the category of ‘satisfactory’ after [Moriassi et al., \(2015\)](#). MSE is measured in units of meter cube per second ( $\text{m}^3\text{s}^{-1}$ ).

Model Type	Flow Type	Training			Validation			Test		
		MSE	NSE	PBIAS	MSE	NSE	PBIAS	MSE	NSE	PBIAS
<b>HSPF</b>	Surface runoff	1.6e-4	-0.27	45.8	4.7e-5	-0.31	69	1.3e-4	0.03	26
	Sub-surface flow	5.4e-4	0.35	-70.8	9.2e-5	<b>0.56</b>	-54	2.9e-4	<b>0.57</b>	-55
	Total discharge	5.7e-4	0.39	-66	1.4e-4	<b>0.56</b>	-47	3.9e-4	<b>0.60</b>	-52
<b>Simple</b>	Surface runoff	8.3e-5	0.43	<b>-5.6</b>	3.5e-5	0.13	-53	5.3e-5	<b>0.65</b>	<b>-3.2</b>
<b>LSTM</b>	Sub-surface flow	5.1e-4	0.47	<b>-14</b>	2.6e-4	-0.12	64	4.9e-4	0.34	-16
	Total discharge	6.0e-4	<b>0.56</b>	<b>-14.4</b>	3.3e-5	0.08	57	5.4e-5	<b>0.51</b>	<b>-15</b>
<b>HRU-based</b>	Surface runoff	1.2e-4	0.18	-63	4.3e-5	-0.06	54	1.4e-4	0.06	-67
<b>LSTM</b>	Sub-surface	3.3e-4	<b>0.66</b>	-22	1.7e-4	0.33	10	2.8e-4	<b>0.63</b>	17
	Total	5.5e-4	<b>0.59</b>	-23	2.7e-4	0.29	<b>7</b>	4.8e-4	<b>0.56</b>	-19

**Table 4** Hyper-parameters and their optimization. The optimization of these parameters was carried out for 5 scenarios. During optimization, parameters such as learning rate, hidden units, and NN layers were varied in the ranges given Table S3. Validation MSE represents the MSE value to which the algorithm converged for each sequence length.

<b>Sequence length</b>	<b>Learning rate</b>	<b>Hidden units</b>	<b>NN layers</b>	<b>Normalization</b>	<b>Loss calculation method</b>	<b>Type of NN cell</b>	<b>Activation function</b>	<b>Validation MSE (m<sup>3</sup>s<sup>-1</sup>)</b>
20	1.164e-6	128	4	True	Weighted	LSTM	ReLu	6.3e-3
30	3.07e-4	128	3	True	Normal	LSTM	ReLu	6.0e-3
40	1.123e-5	128	1	True	Weighted	LSTM	ReLu	6.2e-3
50	1.52e-5	128	1	True	Weighted	LSTM	Tanh	6.5e-3
60	5.441e-5	128	4	True	Normal	LSTM	ReLu	6.4e-3